



CHORUS

This is the accepted manuscript made available via CHORUS. The article has been published as:

Systematic study of azimuthal anisotropy in Cu + Cu and Au + Au collisions at $\sqrt{s_{NN}}=62.4$ and 200 GeV

A. Adare *et al.* (PHENIX Collaboration)

Phys. Rev. C **92**, 034913 — Published 23 September 2015

DOI: [10.1103/PhysRevC.92.034913](https://doi.org/10.1103/PhysRevC.92.034913)

Systematic Study of Azimuthal Anisotropy in Cu+Cu and Au+Au Collisions at

$$\sqrt{s_{NN}}=62.4 \text{ and } 200 \text{ GeV}$$

A. Adare,¹¹ S. Afanasiev,²⁷ C. Aidala,^{12,39} N.N. Ajitanand,⁵⁷ Y. Akiba,^{51,52} H. Al-Bataineh,⁴⁵ A. Al-Jamel,⁴⁵
J. Alexander,⁵⁷ K. Aoki,^{32,51} L. Aphecetche,⁵⁹ R. Armendariz,⁴⁵ S.H. Aronson,⁶ J. Asai,⁵² E.T. Atomssa,³³
R. Averbeck,⁵⁸ T.C. Awes,⁴⁷ B. Azmoun,⁶ V. Babintsev,²¹ G. Baksay,¹⁷ L. Baksay,¹⁷ A. Baldissieri,¹⁴ K.N. Barish,⁷
P.D. Barnes,^{36,*} B. Bassalleck,⁴⁴ S. Bathe,^{4,7} S. Batsouli,^{12,47} V. Baublis,⁵⁰ F. Bauer,⁷ A. Bazilevsky,⁶
S. Belikov,^{6,25,*} R. Bennett,⁵⁸ Y. Berdnikov,⁵⁴ A.A. Bickley,¹¹ M.T. Bjonrdal,¹² J.G. Boissevain,³⁶ H. Borel,¹⁴
K. Boyle,⁵⁸ M.L. Brooks,³⁶ D.S. Brown,⁴⁵ D. Bucher,⁴⁰ H. Buesching,⁶ V. Bumazhnov,²¹ G. Bunce,^{6,52}
J.M. Burward-Hoy,³⁶ S. Butsyk,^{36,58} S. Campbell,⁵⁸ J.-S. Chai,²⁸ B.S. Chang,⁶⁷ J.-L. Charvet,¹⁴ S. Chernichenko,²¹
C.Y. Chi,¹² J. Chiba,²⁹ M. Chiu,^{12,22} I.J. Choi,⁶⁷ T. Chujo,⁶³ P. Chung,⁵⁷ A. Churnyn,²¹ V. Cianciolo,⁴⁷
C.R. Cleven,¹⁹ Y. Cobigo,¹⁴ B.A. Cole,¹² M.P. Comets,⁴⁸ P. Constantin,^{25,36} M. Csanád,¹⁶ T. Csörgő,⁶⁶
T. Dahms,⁵⁸ K. Das,¹⁸ G. David,⁶ M.B. Deaton,¹ K. Dehmelt,¹⁷ H. Delagrange,⁵⁹ A. Denisov,²¹ D. d'Enterria,¹²
A. Deshpande,^{52,58} E.J. Desmond,⁶ O. Dietzsch,⁵⁵ A. Dion,⁵⁸ M. Donadelli,⁵⁵ J.L. Drachenberg,¹ O. Drapier,³³
A. Drees,⁵⁸ A.K. Dubey,⁶⁵ A. Durum,²¹ V. Dzhordzhadze,^{7,60} Y.V. Efremenko,⁴⁷ J. Egdemir,⁵⁸ F. Ellinghaus,¹¹
W.S. Emam,⁷ A. Enokizono,^{20,35} H. En'yo,^{51,52} B. Espagnon,⁴⁸ S. Esumi,⁶² K.O. Eyser,⁷ D.E. Fields,^{44,52}
M. Finger,^{8,27} M. Finger, Jr.,^{8,27} F. Fleuret,³³ S.L. Fokin,³¹ B. Forestier,³⁷ Z. Fraenkel,^{65,*} J.E. Frantz,^{12,46,58}
A. Franz,⁶ A.D. Frawley,¹⁸ K. Fujiwara,⁵¹ Y. Fukao,^{32,51} S.-Y. Fung,⁷ T. Fusayasu,⁴² S. Gadrat,³⁷
I. Garishvili,⁶⁰ F. Gastineau,⁵⁹ M. Germain,⁵⁹ A. Glenn,^{11,60} H. Gong,⁵⁸ M. Gonin,³³ J. Gosset,¹⁴
Y. Goto,^{51,52} R. Granier de Cassagnac,³³ N. Grau,^{2,25} S.V. Greene,⁶³ M. Grosse Perdekamp,^{22,52} T. Gunji,¹⁰
H.-Å. Gustafsson,^{38,*} T. Hachiya,^{20,51} A. Hadj Henni,⁵⁹ C. Haegemann,⁴⁴ J.S. Haggerty,⁶ M.N. Hagiwara,¹
H. Hamagaki,¹⁰ R. Han,⁴⁹ H. Harada,²⁰ E.P. Hartouni,³⁵ K. Haruna,²⁰ M. Harvey,⁶ E. Haslum,³⁸ K. Hasuko,⁵¹
R. Hayano,¹⁰ X. He,¹⁹ M. Heffner,³⁵ T.K. Hemmick,⁵⁸ T. Hester,⁷ J.M. Heuser,⁵¹ H. Hiejima,²² J.C. Hill,²⁵
R. Hobbs,⁴⁴ M. Hohlmann,¹⁷ M. Holmes,⁶³ W. Holzmann,⁵⁷ K. Homma,²⁰ B. Hong,³⁰ T. Horaguchi,^{51,61}
D. Hornback,⁶⁰ S. Huang,⁶³ M.G. Hur,²⁸ T. Ichihara,^{51,52} H. Inuma,^{32,51} K. Imai,^{26,32,51} M. Inaba,⁶²
Y. Inoue,^{51,53} D. Isenhower,¹ L. Isenhower,¹ M. Ishihara,⁵¹ T. Isobe,¹⁰ M. Issah,⁵⁷ A. Isupov,²⁷ B.V. Jacak,⁵⁸
J. Jia,¹² J. Jin,¹² O. Jinnouchi,⁵² B.M. Johnson,⁶ K.S. Joo,⁴¹ D. Jouan,⁴⁸ F. Kajihara,^{10,51} S. Kametani,^{10,64}
N. Kamihara,^{51,61} J. Kamin,⁵⁸ M. Kaneta,⁵² J.H. Kang,⁶⁷ H. Kanou,^{51,61} T. Kawagishi,⁶² D. Kwall,⁵²
A.V. Kazantsev,³¹ S. Kelly,¹¹ A. Khanzadeev,⁵⁰ J. Kikuchi,⁶⁴ D.H. Kim,⁴¹ D.J. Kim,⁶⁷ E. Kim,⁵⁶ Y.-S. Kim,²⁸
E. Kinney,¹¹ Á. Kiss,¹⁶ E. Kistenev,⁶ A. Kiyomichi,⁵¹ J. Klay,³⁵ C. Klein-Boesing,⁴⁰ L. Kochenda,⁵⁰
V. Kochetkov,²¹ B. Komkov,⁵⁰ M. Konno,⁶² D. Kotchetkov,⁷ A. Kozlov,⁶⁵ A. Král,¹³ A. Kravitz,¹²
P.J. Kroon,⁶ J. Kubart,^{8,24} G.J. Kunde,³⁶ N. Kurihara,¹⁰ K. Kurita,^{51,53} M.J. Kweon,³⁰ Y. Kwon,^{60,67}
G.S. Kyle,⁴⁵ R. Lacey,⁵⁷ Y.S. Lai,¹² J.G. Lajoie,²⁵ A. Lebedev,²⁵ Y. Le Bornec,⁴⁸ S. Leckey,⁵⁸ D.M. Lee,³⁶
M.K. Lee,⁶⁷ T. Lee,⁵⁶ M.J. Leitch,³⁶ M.A.L. Leite,⁵⁵ B. Lenzi,⁵⁵ X. Li,⁹ X.H. Li,⁷ H. Lim,⁵⁶ T. Liška,¹³
A. Litvinenko,²⁷ M.X. Liu,³⁶ B. Love,⁶³ D. Lynch,⁶ C.F. Maguire,⁶³ Y.I. Makdisi,^{5,6} A. Malakhov,²⁷ M.D. Malik,⁴⁴
V.I. Manko,³¹ Y. Mao,^{49,51} L. Mašek,^{8,24} H. Masui,⁶² F. Matathias,^{12,58} M.C. McCain,²² M. McCumber,⁵⁸
P.L. McGaughey,³⁶ Y. Miake,⁶² P. Mikeš,^{8,24} K. Miki,⁶² T.E. Miller,⁶³ A. Milov,⁵⁸ S. Mioduszewski,⁶
G.C. Mishra,¹⁹ M. Mishra,³ J.T. Mitchell,⁶ M. Mitrovski,⁵⁷ A. Morreale,⁷ D.P. Morrison,^{6,†} J.M. Moss,³⁶
T.V. Moukhanova,³¹ D. Mukhopadhyay,⁶³ J. Murata,^{51,53} S. Nagamiya,^{29,51} Y. Nagata,⁶² J.L. Nagle,^{11,‡}
M. Naglis,⁶⁵ I. Nakagawa,^{51,52} Y. Nakamiya,²⁰ T. Nakamura,²⁰ K. Nakano,^{51,61} J. Newby,³⁵ M. Nguyen,⁵⁸
B.E. Norman,³⁶ R. Nouicer,⁶ A.S. Nyanin,³¹ J. Nystrand,³⁸ E. O'Brien,⁶ S.X. Oda,¹⁰ C.A. Ogilvie,²⁵ H. Ohnishi,⁵¹
I.D. Ojha,⁶³ M. Oka,⁶² K. Okada,⁵² O.O. Omiwade,¹ A. Oskarsson,³⁸ I. Otterlund,³⁸ M. Ouchida,²⁰ K. Ozawa,¹⁰
R. Pak,⁶ D. Pal,⁶³ A.P.T. Palounek,³⁶ V. Pantuev,^{23,58} V. Papavassiliou,⁴⁵ J. Park,⁵⁶ W.J. Park,³⁰ S.F. Pate,⁴⁵
H. Pei,²⁵ J.-C. Peng,²² H. Pereira,¹⁴ V. Peresedov,²⁷ D.Yu. Peressounko,³¹ C. Pinkenburg,⁶ R.P. Pisani,⁶
M.L. Purschke,⁶ A.K. Purwar,^{36,58} H. Qu,¹⁹ J. Rak,^{25,44} A. Rakotozafindrabe,³³ I. Ravinovich,⁶⁵ K.F. Read,^{47,60}
S. Rembeczki,¹⁷ M. Reuter,⁵⁸ K. Reygers,⁴⁰ V. Riabov,^{43,50} Y. Riabov,⁵⁰ G. Roche,³⁷ A. Romana,^{33,*} M. Rosati,²⁵
S.S.E. Rosendahl,³⁸ P. Rosnet,³⁷ P. Rukoyatkin,²⁷ V.L. Rykov,⁵¹ S.S. Ryu,⁶⁷ B. Sahlmueller,^{40,58} N. Saito,^{32,51,52}
T. Sakaguchi,^{6,10,64} S. Sakai,⁶² H. Sakata,²⁰ V. Samsonov,^{43,50} H.D. Sato,^{32,51} S. Sato,^{6,26,29} S. Sawada,²⁹
J. Seele,¹¹ R. Seidl,²² V. Semenov,²¹ R. Seto,⁷ D. Sharma,⁶⁵ T.K. Shea,⁶ I. Shein,²¹ A. Shevel,^{50,57}
T.-A. Shibata,^{51,61} K. Shigaki,²⁰ M. Shimomura,⁶² T. Shohjoh,⁶² K. Shoji,^{32,51} A. Sickles,^{22,58} C.L. Silva,⁵⁵
D. Silvermyr,⁴⁷ C. Silvestre,¹⁴ K.S. Sim,³⁰ C.P. Singh,³ V. Singh,³ S. Skutnik,²⁵ M. Slunečka,^{8,27} W.C. Smith,¹
A. Soldatov,²¹ R.A. Soltz,³⁵ W.E. Sondheim,³⁶ S.P. Sorensen,⁶⁰ I.V. Sourikova,⁶ F. Staley,¹⁴ P.W. Stankus,⁴⁷
E. Stenlund,³⁸ M. Stepanov,^{45,*} A. Ster,⁶⁶ S.P. Stoll,⁶ T. Sugitate,²⁰ C. Suire,⁴⁸ J.P. Sullivan,³⁶ J. Sziklai,⁶⁶

53 T. Tabaru,⁵² S. Takagi,⁶² E.M. Takagui,⁵⁵ A. Taketani,^{51,52} K.H. Tanaka,²⁹ Y. Tanaka,⁴² K. Tanida,^{51,52,56}
 54 M.J. Tannenbaum,⁶ A. Taranenko,^{43,57} P. Tarján,¹⁵ T.L. Thomas,⁴⁴ T. Todoroki,^{51,62} M. Togawa,^{32,51} A. Toia,⁵⁸
 55 J. Tojo,⁵¹ L. Tomášek,²⁴ H. Torii,⁵¹ R.S. Towell,¹ V-N. Tram,³³ I. Tserruya,⁶⁵ Y. Tsuchimoto,^{20,51}
 56 S.K. Tuli,^{3,*} H. Tydesjö,³⁸ N. Tyurin,²¹ C. Vale,²⁵ H. Valle,⁶³ H.W. van Hecke,³⁶ J. Velkovska,⁶³ R. Vértesi,¹⁵
 57 A.A. Vinogradov,³¹ M. Virius,¹³ V. Vrba,²⁴ E. Vznuzdaev,⁵⁰ M. Wagner,^{32,51} D. Walker,⁵⁸ X.R. Wang,⁴⁵
 58 Y. Watanabe,^{51,52} J. Wessels,⁴⁰ S.N. White,⁶ N. Willis,⁴⁸ D. Winter,¹² C.L. Woody,⁶ M. Wysocki,¹¹ W. Xie,^{7,52}
 59 Y.L. Yamaguchi,⁶⁴ A. Yanovich,²¹ Z. Yasin,⁷ J. Ying,¹⁹ S. Yokkaichi,^{51,52} G.R. Young,⁴⁷ I. Younus,^{34,44}
 60 I.E. Yushmanov,³¹ W.A. Zajc,¹² O. Zaudtke,⁴⁰ C. Zhang,^{12,47} S. Zhou,⁹ J. Zimányi,^{66,*} and L. Zolin²⁷

(PHENIX Collaboration)

¹Abilene Christian University, Abilene, Texas 79699, USA

²Department of Physics, Augustana College, Sioux Falls, South Dakota 57197, USA

³Department of Physics, Banaras Hindu University, Varanasi 221005, India

⁴Baruch College, City University of New York, New York, New York, 10010 USA

⁵Collider-Accelerator Department, Brookhaven National Laboratory, Upton, New York 11973-5000, USA

⁶Physics Department, Brookhaven National Laboratory, Upton, New York 11973-5000, USA

⁷University of California - Riverside, Riverside, California 92521, USA

⁸Charles University, Ovocný trh 5, Praha 1, 116 36, Prague, Czech Republic

⁹Science and Technology on Nuclear Data Laboratory, China Institute of Atomic Energy, Beijing 102413, People's Republic of China

¹⁰Center for Nuclear Study, Graduate School of Science, University of Tokyo, 7-3-1 Hongo, Bunkyo, Tokyo 113-0033, Japan

¹¹University of Colorado, Boulder, Colorado 80309, USA

¹²Columbia University, New York, New York 10027 and Nevis Laboratories, Irvington, New York 10533, USA

¹³Czech Technical University, Zikova 4, 166 36 Prague 6, Czech Republic

¹⁴Dapnia, CEA Saclay, F-91191, Gif-sur-Yvette, France

¹⁵Debrecen University, H-4010 Debrecen, Egyetem tér 1, Hungary

¹⁶ELTE, Eötvös Loránd University, H-1117 Budapest, Pázmány Péter sétány 1/A, Hungary

¹⁷Florida Institute of Technology, Melbourne, Florida 32901, USA

¹⁸Florida State University, Tallahassee, Florida 32306, USA

¹⁹Georgia State University, Atlanta, Georgia 30303, USA

²⁰Hiroshima University, Kagamiyama, Higashi-Hiroshima 739-8526, Japan

²¹IHEP Protvino, State Research Center of Russian Federation, Institute for High Energy Physics, Protvino, 142281, Russia

²²University of Illinois at Urbana-Champaign, Urbana, Illinois 61801, USA

²³Institute for Nuclear Research of the Russian Academy of Sciences, prospekt 60-letiya Oktyabrya 7a, Moscow 117312, Russia

²⁴Institute of Physics, Academy of Sciences of the Czech Republic, Na Slovance 2, 182 21 Prague 8, Czech Republic

²⁵Iowa State University, Ames, Iowa 50011, USA

²⁶Advanced Science Research Center, Japan Atomic Energy Agency, 2-4 Shirakata Shirane, Tokai-mura, Naka-gun, Ibaraki-ken 319-1195, Japan

²⁷Joint Institute for Nuclear Research, 141980 Dubna, Moscow Region, Russia

²⁸KAERI, Cyclotron Application Laboratory, Seoul, Korea

²⁹KEK, High Energy Accelerator Research Organization, Tsukuba, Ibaraki 305-0801, Japan

³⁰Korea University, Seoul, 136-701, Korea

³¹Russian Research Center "Kurchatov Institute," Moscow, 123098 Russia

³²Kyoto University, Kyoto 606-8502, Japan

³³Laboratoire Leprince-Ringuet, Ecole Polytechnique, CNRS-IN2P3, Route de Saclay, F-91128, Palaiseau, France

³⁴Physics Department, Lahore University of Management Sciences, Lahore 54792, Pakistan

³⁵Lawrence Livermore National Laboratory, Livermore, California 94550, USA

³⁶Los Alamos National Laboratory, Los Alamos, New Mexico 87545, USA

³⁷LPC, Université Blaise Pascal, CNRS-IN2P3, Clermont-Fd, 63177 Aubiere Cedex, France

³⁸Department of Physics, Lund University, Box 118, SE-221 00 Lund, Sweden

³⁹Department of Physics, University of Michigan, Ann Arbor, Michigan 48109-1040, USA

⁴⁰Institut für Kernphysik, University of Muenster, D-48149 Muenster, Germany

⁴¹Myongji University, Yongin, Kyonggido 449-728, Korea

⁴²Nagasaki Institute of Applied Science, Nagasaki-shi, Nagasaki 851-0193, Japan

⁴³National Research Nuclear University, MEPhI, Moscow Engineering Physics Institute, Moscow, 115409, Russia

⁴⁴University of New Mexico, Albuquerque, New Mexico 87131, USA

⁴⁵New Mexico State University, Las Cruces, New Mexico 88003, USA

⁴⁶Department of Physics and Astronomy, Ohio University, Athens, Ohio 45701, USA

⁴⁷Oak Ridge National Laboratory, Oak Ridge, Tennessee 37831, USA

⁴⁸IPN-Orsay, Université Paris Sud, CNRS-IN2P3, BP1, F-91406, Orsay, France

⁴⁹Peking University, Beijing 100871, People's Republic of China

⁵⁰PNPI, Petersburg Nuclear Physics Institute, Gatchina, Leningrad Region, 188300, Russia

⁵¹RIKEN Nishina Center for Accelerator-Based Science, Wako, Saitama 351-0198, Japan

115 ⁵²RIKEN BNL Research Center, Brookhaven National Laboratory, Upton, New York 11973-5000, USA

116 ⁵³Physics Department, Rikkyo University, 3-34-1 Nishi-Ikebukuro, Toshima, Tokyo 171-8501, Japan

117 ⁵⁴Saint Petersburg State Polytechnic University, St. Petersburg, 195251 Russia

118 ⁵⁵Universidade de São Paulo, Instituto de Física, Caixa Postal 66318, São Paulo CEP05315-970, Brazil

119 ⁵⁶Department of Physics and Astronomy, Seoul National University, Seoul 151-742, Korea

120 ⁵⁷Chemistry Department, Stony Brook University, SUNY, Stony Brook, New York 11794-3400, USA

121 ⁵⁸Department of Physics and Astronomy, Stony Brook University, SUNY, Stony Brook, New York 11794-3800, USA

122 ⁵⁹SUBATECH (Ecole des Mines de Nantes, CNRS-IN2P3, Université de Nantes) BP 20722 - 44307, Nantes, France

123 ⁶⁰University of Tennessee, Knoxville, Tennessee 37996, USA

124 ⁶¹Department of Physics, Tokyo Institute of Technology, Oh-okayama, Meguro, Tokyo 152-8551, Japan

125 ⁶²Institute of Physics, University of Tsukuba, Tsukuba, Ibaraki 305, Japan

126 ⁶³Vanderbilt University, Nashville, Tennessee 37235, USA

127 ⁶⁴Waseda University, Advanced Research Institute for Science and
128 Engineering, 17 Kikui-cho, Shinjuku-ku, Tokyo 162-0044, Japan

129 ⁶⁵Weizmann Institute, Rehovot 76100, Israel

130 ⁶⁶Institute for Particle and Nuclear Physics, Wigner Research Centre for Physics, Hungarian
131 Academy of Sciences (Wigner RCP, RMKI) H-1525 Budapest 114, POBox 49, Budapest, Hungary

132 ⁶⁷Yonsei University, IPAP, Seoul 120-749, Korea

133 We have studied the dependence of azimuthal anisotropy v_2 for inclusive and identified charged
134 hadrons in Au+Au and Cu+Cu collisions on collision energy, species, and centrality. The values of v_2
135 as a function of transverse momentum p_T and centrality in Au+Au collisions at $\sqrt{s_{NN}}=200$ GeV and
136 62.4 GeV are the same within uncertainties. However, in Cu+Cu collisions we observe a decrease in
137 v_2 values as the collision energy is reduced from 200 to 62.4 GeV. The decrease is larger in the more
138 peripheral collisions. By examining both Au+Au and Cu+Cu collisions we find that v_2 depends both
139 on eccentricity and the number of participants, N_{part} . We observe that v_2 divided by eccentricity (ε)
140 monotonically increases with N_{part} and scales as $N_{\text{part}}^{1/3}$. The Cu+Cu data at 62.4 GeV falls below
141 the other scaled v_2 data. For identified hadrons, v_2 divided by the number of constituent quarks n_q
142 is independent of hadron species as a function of transverse kinetic energy $KE_T = m_T - m$ between
143 $0.1 < KE_T/n_q < 1$ GeV. Combining all of the above scaling and normalizations, we observe a
144 near-universal scaling, with the exception of the Cu+Cu data at 62.4 GeV, of $v_2/(n_q \cdot \varepsilon \cdot N_{\text{part}}^{1/3})$ vs
145 KE_T/n_q for all measured particles.

146 PACS numbers: 25.75.Dw

* Deceased

† PHENIX Co-Spokesperson: morrison@bnl.gov

‡ PHENIX Co-Spokesperson: jamie.nagle@colorado.edu

I. INTRODUCTION

The azimuthal anisotropy of particles produced in relativistic heavy ion collisions is a powerful probe for investigating the characteristics of the quark-gluon plasma (QGP) [1–4]. The elliptic azimuthal anisotropy (v_2) is defined by the amplitude of the second-order harmonic in a Fourier series expansion of emitted particle azimuthal distributions:

$$v_2 = \langle \cos(2[\phi - \Psi_{\text{RP}}]) \rangle, \quad (1)$$

where ϕ represents the azimuthal emission angle of a particle and Ψ_{RP} is the azimuthal angle of the reaction plane, which is defined by the impact parameter and the beam axis. The brackets denote statistical averaging over particles and events. Elliptic flow is sensitive to the early stage of heavy ion collisions because pressure gradients transfer the initial geometrical anisotropy of the collision region to an anisotropy in momentum space.

One of the most remarkable findings at the Relativistic Heavy Ion Collider (RHIC) is that the strength of v_2 [5] is much larger than what is expected from a hadronic scenario [6]. Moreover, a scaling of v_2 by the number of constituent quarks in a hadron in the intermediate transverse momentum region ($p_T = 1\text{--}4$ GeV/ c) has been found for a broad range of particle species produced in Au+Au at $\sqrt{s_{NN}} = 200$ GeV [7, 8]. Both STAR and PHENIX experiments have observed that v_2 scales better as a function of the transverse kinetic energy of the hadron. These scalings of v_2 are consistent with constituent quark flow at early collision times and recombination as the dominant process of hadronization.

The detailed interpretation of v_2 results requires modeling [9, 10] of the wavefunction of the incoming nuclei, fluctuations of the initial geometry, viscous relativistic hydrodynamics, hadronic freeze out and subsequent rescattering, along with various model parameters such as the assumed equation of state and transport coefficients, e.g. viscosity. In recent calculations, the strength of v_2 for hadrons in heavy ion collisions at $\sqrt{s_{NN}} = 200$ GeV can be reproduced by hydrodynamical models that include shear viscosity and initial fluctuations [11–13].

At the LHC, experiments have measured v_2 as a function of p_T from Pb+Pb collisions at an order of magnitude higher beam energy, at $\sqrt{s_{NN}} = 2.76$ TeV [14–16]. These v_2 results as a function of p_T for inclusive hadrons are very similar in magnitude and shape to the RHIC measurements at 200 GeV. However, the v_2 measurements for identified hadrons at LHC [17, 18] below 3 GeV/ c do not scale well with the quark number and transverse kinetic energy of the hadron with deviations up to 40%.

A comparison of measured v_2 at the lower beam energies at RHIC ($\sqrt{s_{NN}} = 7.7\text{--}200$ GeV) shows that v_2 as a function of p_T seems to be saturated above $\sqrt{s_{NN}} = 39$ GeV and decreases below this beam energy [19]. The scaling of v_2 with transverse kinetic energy is broken below a beam energy of 19 GeV [19]. Possible explanations for this behavior include rescattering in the later hadronic phase, incomplete thermalization in the initial stage, or the plasma not being formed at these lower beam energies.

Because transverse kinetic energy scaling is broken at energies significantly lower and higher than RHIC's full energy of 200 GeV, it is important to provide systematic measurements of v_2 for identified hadrons as a function of system size, collision energy, and centrality. These systematics are needed in order to make progress on the nature of the QGP at lower energy-density. We report on such a set of measurements in this paper, examining both Au+Au and Cu+Cu collisions at 200 GeV and 62.4 GeV beam energies. This adds to the low-energy Au+Au measurements made by STAR [19] and their Cu+Cu v_2 data at 200 GeV and 62.4 GeV beam energies [20]. The system size dependence of flow is particularly important because long-range azimuthal correlations have also been observed in high-multiplicity events from much smaller systems such as d +Au collisions [21] at RHIC, p + p [22], and p +Pb collisions [23] at LHC. The origin of these anisotropies is currently unknown; various competing explanations include parton saturation and hydrodynamic flow.

We expect that the systematic study of v_2 for inclusive and identified particles can provide information on the temperature dependence of η/s (*i.e.* the ratio of shear viscosity to entropy density s), the impact of viscosity on systems of different sizes, as well as constraining models of the reaction dynamics.

The organization of this paper is as follows: Section II describes the PHENIX detector used for this analysis, Section III describes the experimental method of azimuthal anisotropy analysis, Section IV presents the results of the systematic study for inclusive charged hadron v_2 , and Section V presents the results of the systematic study for the v_2 of identified charged hadrons. The new data published in this paper are the Cu+Cu data at 62.4 GeV, as well the Au+Au v_2 results for $p_T > 5$ GeV/ c . Other data come from prior PHENIX publications. [7, 24]

II. PHENIX DETECTOR

The results that we present in this paper were obtained with the PHENIX detector at RHIC [25]. We discuss below the main detector components that were used for this analysis.

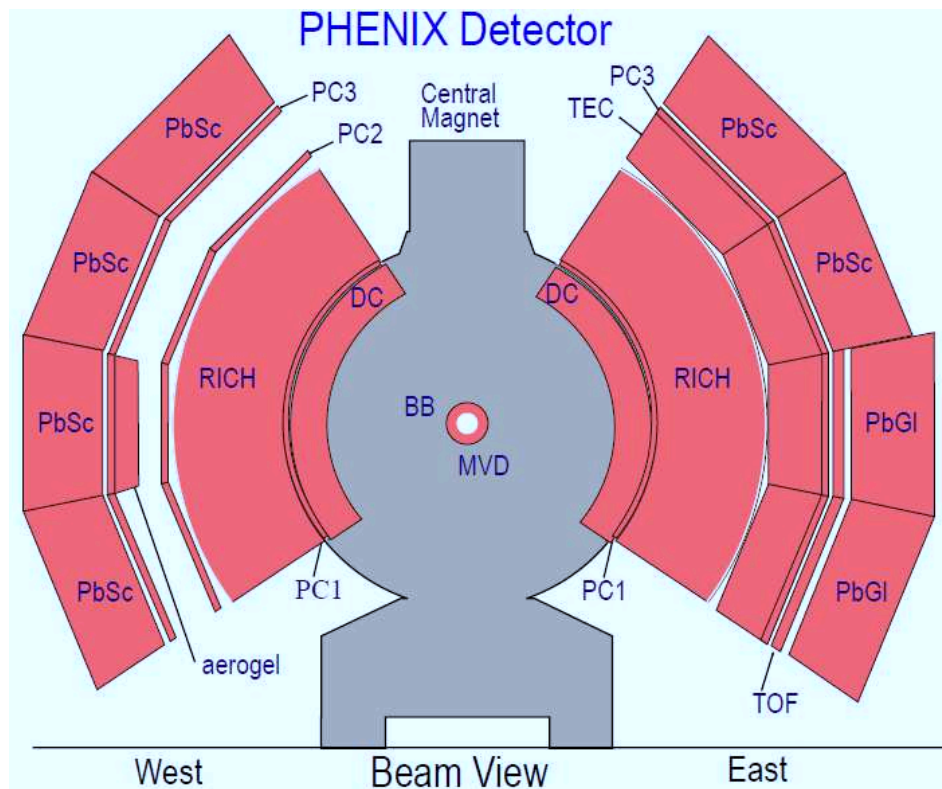


FIG. 1. (Color online) Installed and active detectors for the RUN-4 configuration of the PHENIX experiment. Shown are the two central spectrometer arms viewed in a cut through the collision vertex.

198

A. Global Detectors

199 The Beam-Beam Counters (BBCs) are located 144 cm upstream and downstream of the beam crossing point. Each
 200 BBC comprises 64 individual quartz Čerenkov counters and covers the full azimuthal angle in the pseudorapidity
 201 range $3.0 < |\eta| < 3.9$. The average of the times measured by the two BBCs from fast leading particles provide the
 202 start time for the event, while the difference in times provides the vertex position of the collision. The timing and
 203 position resolution of the BBCs are 20 ps and 0.6 cm respectively for both Au+Au and Cu+Cu collisions. The event
 204 start time is also used for particle identification through the time-of-flight to the TOF and EMCal subsystems in the
 205 PHENIX central arms.

206 The Zero Degree Calorimeters (ZDCs) cover the pseudorapidity range $|\eta| > 6$ and measure the energy of spectator
 207 neutrons with an energy resolution of approximately 20%. More details about these detectors can be found in [26].

208

B. Central-arm tracking detectors

209 Two (identical) Drift Chambers (DC) are installed in the east and west arms of the PHENIX central detector and
 210 are located between 2.02 and 2.46 m radial distance from the interaction point. Each of the two drift chambers extends
 211 180 cm along the beam direction and subtends $\pi/2$ in azimuth. The momentum resolution for tracks reconstructed by
 212 the DC is $0.7\% \oplus 1.1\% p$ (GeV/c). The position of the DCs relative to the other detectors in the central spectrometer
 213 is shown in Fig. 1 and details of the DC construction and tracking performance can be found in [27].

214 The PHENIX pad chambers (PC) are multi-wire proportional chambers composed of three separate layers of pixel
 215 detectors. Each pad chamber detector contains a single plane of wires in a gas volume bounded by two cathode
 216 planes. The innermost pad chamber plane, PC1, is located between the DC and a ring-imaging Čerenkov counter
 217 (RICH) on both East and West arms, PC2 is placed in back of the RICH on the West arm only, and PC3 is located
 218 in front of the Electromagnetic Calorimeters on both East and West arms.

219 The PC system determines space points outside the magnetic field and hence provides straight-line particle trajec-
 220 tories. They are the only nonprojective detectors in the central tracking system and thus are critical elements of the

221 pattern recognition. PC1 is also essential for determining the three-dimensional momentum vector by providing the
 222 z coordinate of each track at the exit of the DC. Details of the PC construction and their performance can be found
 223 in [27].

224

C. Time-of-flight counters

225 The PHENIX time-of-flight (TOF) detector serves as a particle identification device for charged hadrons. The time
 226 resolution for the BBC-TOF system is around 120 ps, which enables 2σ separation of π/K up to 2.0 GeV/ c . The
 227 length of the flight path of each track from the event vertex to the TOF detector is calculated by the momentum
 228 reconstruction algorithm. The length and time of flight are combined to identify the charged particles. The TOF is
 229 located between the PC3 and EMCal in the east arm and about 5.06 m away from the collision vertex. It covers $|\eta|$
 230 < 0.35 and azimuthal angle, $\Delta\phi = 45^\circ$. Details of the TOF construction and performance can be found in [26].

231

D. Electromagnetic calorimeter

232 The PHENIX EMCal was designed to measure the spatial position and energy of electrons and photons produced
 233 in heavy ion collisions. The EMCal covers the full central spectrometer acceptance of $|\eta| < 0.35$ and is installed in
 234 both arms, each subtending 90° in azimuth, i.e. larger than the TOF acceptance. The EMCal comprises six sectors
 235 of lead-scintillator (PbSc) calorimeters and two sectors of lead-glass (PbGl) calorimeters. The PbGl is not used in
 236 this analysis, but we note that the TOF detector is in front of the PbGl so no PID coverage is lost. The PbSc is a
 237 sampling calorimeter and has a timing resolution of 400 ps for hadrons. The PbSc can be used to separate π/K with
 238 2σ up to 1.0 GeV/ c . Details of the PbSc construction and performance are described in [28].

239

E. RICH

240 A Ring Imaging Čerenkov Counter (RICH) is installed on each of the PHENIX central arms. Each RICH detector
 241 is a threshold gas Čerenkov detector with a high angular segmentation filled with CO₂ gas. In this analysis we use
 242 the RICH to reject electrons by removing tracks that match to a RICH ring. It is noted that charged pions with p_T
 243 larger than 4 GeV/ c also radiate in the CO₂ gas.

244

III. EXPERIMENTAL METHOD

245

A. Data sets and event selection

246 We measured Cu+Cu and Au+Au collisions at $\sqrt{s_{NN}} = 62.4$ and 200 GeV. The Cu+Cu data were taken during
 247 RHIC Run-5 (2005) and Au+Au data were taken during RHIC Run-4 (2004) running periods. We used a minimum
 248 bias trigger that was defined by a coincidence between the two BBCs and an energy threshold of one neutron in both
 249 ZDCs. The collision vertex along the beam direction, z , was measured by the BBC. The total number of minimum
 250 bias events that were analyzed after requiring an offline vertex cut of $|z| < 30$ cm and selecting good runs are listed
 251 in Table I.

TABLE I. Information on the data sets and event statistics.

Year	Species	Energy [GeV]	# of events
2004	Au+Au	200	8.2×10^8
2004	Au+Au	62.4	2.6×10^7
2005	Cu+Cu	200	8.0×10^8
2005	Cu+Cu	62.4	3.4×10^8

252 In Au+Au collisions at 200 GeV the centrality of the collision was determined by using the correlation of the
 253 total energy deposited in the ZDCs with the total charge deposited in the BBCs, as described in [29]. However, in
 254 200 GeV Cu+Cu, 62.4 GeV Cu+Cu, and 62.4 GeV Au+Au collisions, the resolving power of the ZDCs is insufficient

255 to significantly contribute to the centrality definition. Therefore, the total charge deposited in the BBCs is used to
 256 determine centrality in these collision systems, as described in [29]. A Glauber model Monte-Carlo simulation of
 257 the each collision [30, 31] was used to estimate the average number of participating nucleons N_{part} and participant
 258 eccentricity (ε). This simulation includes modeling of the BBC and ZDC response. The eccentricity ε is also known
 259 as the participant eccentricity and includes the effect of fluctuation from the initial participant geometry. Table II
 260 summarizes N_{part} , its systematic uncertainties (ΔN_{part}), ε and its systematic uncertainties ($\Delta\varepsilon$).

TABLE II. Number of participants (N_{part}), its uncertainty (ΔN_{part}), participant eccentricity (ε) and its uncertainty ($\Delta\varepsilon$) from Glauber Monte-Carlo calculations for Au+Au and Cu+Cu collisions at 200 and 62.4 GeV.

centrality bin	Au+Au 200 GeV				Au+Au 62.4 GeV				Cu+Cu 200 GeV				Cu+Cu 62.4 GeV			
	N_{part}	ΔN_{part}	ε	$\Delta\varepsilon$ [%]	N_{part}	ΔN_{part}	ε	$\Delta\varepsilon$ [%]	N_{part}	ΔN_{part}	ε	$\Delta\varepsilon$ [%]	N_{part}	ΔN_{part}	ε	$\Delta\varepsilon$ [%]
0%–10%	325.2	3.3	0.103	2.6	320.7	7.9	0.107	2.3	98.2	2.4	0.163	2.0	93.3	2.6	0.169	1.7
10%–20%	234.6	4.7	0.200	2.5	230.7	9.2	0.207	2.2	73.6	2.5	0.241	3.0	71.1	2.4	0.248	2.6
20%–30%	166.6	5.4	0.284	2.1	163.2	7.6	0.292	2.0	53.0	1.9	0.317	1.9	51.3	2.0	0.324	1.9
30%–40%	114.2	4.4	0.356	1.7	113.0	5.6	0.365	1.8	37.3	1.6	0.401	1.9	36.2	1.8	0.408	1.6
40%–50%	74.4	3.8	0.422	1.5	74.5	4.1	0.431	1.3	25.4	1.3	0.484	1.6	24.9	1.5	0.494	2.1
50%–60%	45.5	3.3	0.491	1.1	45.9	3.1	0.498	1.0	16.7	0.9	0.579	1.4	16.1	0.9	0.587	1.5
60%–70%	25.7	3.8	0.567	0.7	25.9	1.7	0.573	0.8	10.4	0.6	0.674	2.1			0.696	2.3
70%–80%	13.4	3.0	0.666	1.2			0.678	1.1	6.4	0.5	0.721	1.7			0.742	1.6
80%–90%			0.726	2.8			0.740	2.2			0.856	7.2			0.867	6.2

B. Track selection

262 The analysis was performed for inclusive charged hadrons over the transverse momentum range $0.2 < p_T <$
 263 $10 \text{ GeV}/c$, and for identified charged particles (pions ($\pi^+ + \pi^-$), kaons ($K^+ + K^-$), and protons ($p + \bar{p}$)) in the
 264 momentum range up to p_T 2.2, 3, and 4 GeV/c respectively.

265 The track reconstruction procedure is described in [32]. Tracks reconstructed by the DC which do not originate
 266 from the event vertex have been investigated as background to the inclusive charged particle measurement. The main
 267 background sources include secondary particles from hadron decays and e^+e^- pairs from the conversion of photons in
 268 the material between the vertex and the DC [33]. To minimize background originating from the magnets, reconstructed
 269 tracks are required to have a z -position less than $\pm 80 \text{ cm}$ when the tracks cross the outer radius of the DC. The DC
 270 is outside the central magnet field hence we can approximate reconstructed tracks through the central-arm detectors
 271 as straight lines. This enables tracks to be projected to outer detectors and matched to measured hits. Good tracks
 272 are required to be matched to a hit in the PC3, as well as in the EMCal, within 2.5σ of the expected hit location in
 273 both azimuthal and beam directions.

274 The Ring Imaging Čerenkov detector (RICH) also reduces the conversion background. For tracks with $p_T < 4 \text{ GeV}/c$
 275 we apply a cut of $n_0 < 0$ where n_0 is the number of fired phototubes in the RICH ring. For $p_T > 4 \text{ GeV}/c$, we require
 276 tracks to have $E/p > 0.2$, where E denotes the energy deposited in the EMCal and p_T is the transverse momentum of
 277 particles measured in the DC. Because most of the background from photon conversion are low-momentum particles
 278 that were incorrectly reconstructed at higher momentum, when we require a large deposit of energy in the EMCal
 279 this suppresses the conversion background [34].

280 To demonstrate the effectiveness of the E/p cut, Fig. 2 shows the track/hit matching distributions $d\phi/\sigma$ at PC3,
 281 where $d\phi$ is the residual between the track projection point and the detector hit position along ϕ and σ is the standard
 282 deviation of the $d\phi$ distribution. The left panel shows the $d\phi/\sigma$ without an E/p cut, and the right panel shows the
 283 distribution with a cut of $E/p > 0.2$. Note that the vertical scale between the panels is different. The $E/p > 0.2$
 284 cut substantially reduces the background for high p_T tracks. The residual background remaining after these cuts has
 285 been estimated by the fitting the $d\phi/\sigma$ distributions in PC3 with a double Gaussian function (signal and background).
 286 The signal and residual background distributions are required to have the same mean. For $p_T < 4 \text{ GeV}/c$ the residual
 287 background is less than 5% of the real tracks and reaches 10% for p_T 8-10 GeV/c . The efficiency of the $E/p > 0.2$
 288 cut is 0.3 at $p_T = 5 - 6 \text{ GeV}/c$ and 0.1 at $p_T = 7 - 9 \text{ GeV}/c$.

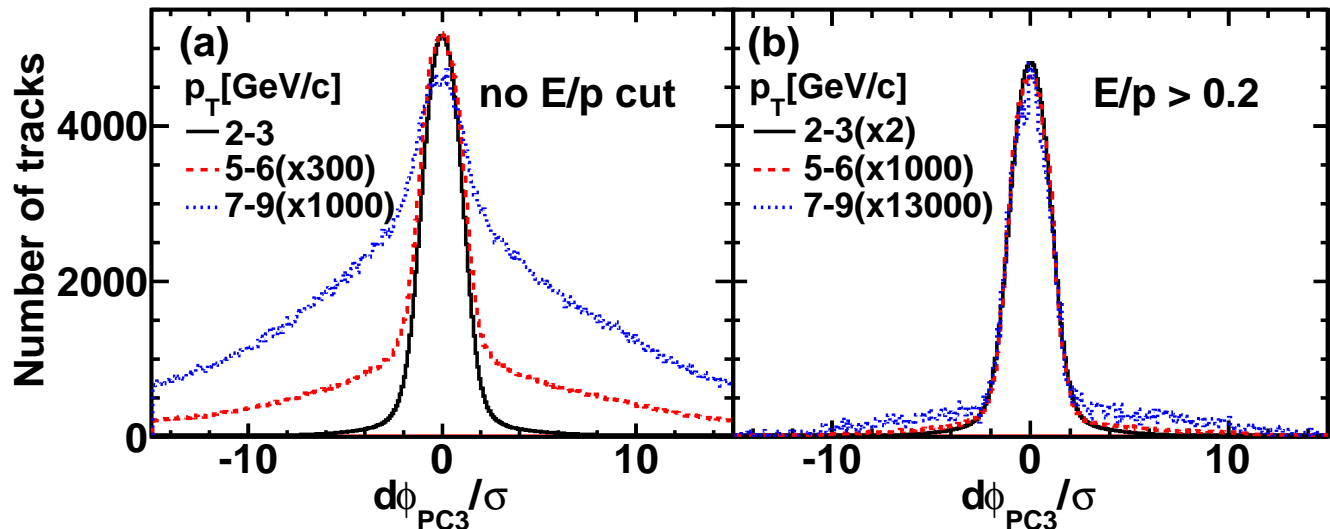


FIG. 2. (Color online) (a) track/hit matching distribution of $d\phi/\sigma$ at PC3 without E/p cut for indicated p_T bins; (b) same quantity, but after applying an $E/p > 0.2$ cut.

289

C. Particle identification

For identified charged hadrons we also require the tracks to have a hit in the TOF detector or EMCal within at most 2σ of the expected hit location in both azimuthal and beam directions. Particles are identified by their mass-squared, using the momentum measurement from the DC (p), time-of-flight between BBC and TOF/EMCal (t), and flight path length (L) from the collision vertex point to the hit position on the TOF wall or cluster in the EMCal. The square of the particle's mass is calculated as

$$m^2 = \frac{p^2}{c^2} \left[\left(\frac{t}{L/c} \right)^2 - 1 \right] \quad (2)$$

The timing resolution of the BBC-TOF and BBC-EMCal systems was determined by examining the timing difference between the measured flight-time t and $t_{\pi\text{expected}}$, the time which is expected under the assumption that the particles are pions. The resulting time distribution is shown in Fig. 3. A narrow peak centered around $t - t_{\pi\text{expected}} \approx 0$ corresponds to pions, and the other two broad peaks are kaons and protons. A Gaussian distribution is fit to the pion peak and yields a resolution of ~ 120 ps for the BBC-TOF system and ~ 400 ps for the BBC-EMCal system.

The PID is performed by applying momentum-dependent cuts in mass-squared (m^2). The m^2 distributions are fit with a 3-Gaussian function corresponding to pions, kaons, and protons. The corresponding widths and centroids are extracted from the data as a function of transverse momentum. To select candidate tracks of a particle species, the m^2 is required to be within two standard deviations of the mean for the selected particles species and outside 2.5 standard deviations of the mean for the other particle species. This provides a sample for each particle species with at least 90% purity in PID. For the BBC-TOF system the upper momentum cutoff is 2.2 GeV/c for kaons and 3 GeV/c for pions. For protons the upper momentum cutoff is 4 GeV/c. For the BBC-EMCal system the upper momentum cutoff is 1 GeV/c for kaons and 1.4 GeV/c for pions. For protons the upper momentum cutoff is 2.2 GeV/c. The lower momentum cutoff for both PID systems is 0.2 GeV/c for pions, 0.3 GeV/c for kaons and 0.5 GeV/c for protons. The PID results for the 200 GeV Au+Au data set were obtained using TOF detector only; for the 62.4 GeV Au+Au and 200 GeV Cu+Cu data sets the PID results were obtained by including identified particles from either the TOF or EMCal over different momentum ranges. For overlap region, we use BBC-EMC because of the better statistics and include the differences between BBC-EMC and BBC-TOF as systematic uncertainty shown in Tab. VI. No correction is applied for any contamination from misidentified hadrons.

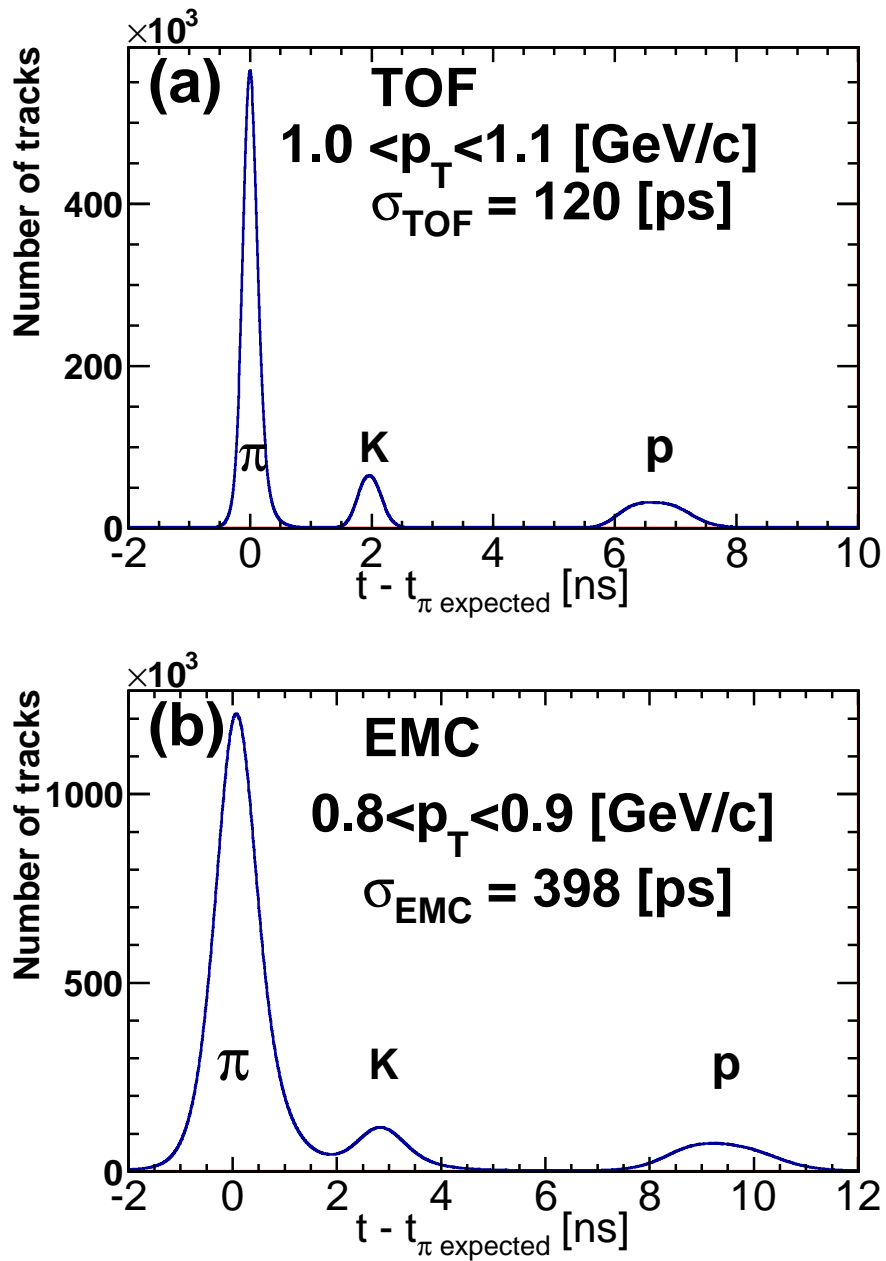


FIG. 3. (Color online) Distributions of $t - t_{\pi \text{ expected}}$, the difference between the measured time-of-flight in the TOF (upper) and EMC (lower) and the time calculated assuming each candidate track is a pion. Resolutions are $\sigma_T \sim 120$ ps for TOF and $\sigma_T \sim 400$ ps for EMC in Au+Au at 200 GeV data.

314

D. Azimuthal anisotropy: event plane method

Because the principal axis of the participants cannot be measured directly in the experiment, the azimuthal angle of the reaction plane is estimated [35]. The estimated reaction plane is called the “event plane” and is determined for each harmonic of the Fourier expansion of the azimuthal distribution. The event flow vector $\vec{Q}_n = (Q_x, Q_y)$ and azimuth of the event plane Ψ_n for n -th harmonic of the azimuthal anisotropy can be expressed as

$$Q_x \equiv |\vec{Q}_n| \cos(n\Psi_n) = \sum_i^M w_i \cos(n\phi_i), \quad (3)$$

$$Q_y \equiv |\vec{Q}_n| \sin(n\Psi_n) = \sum_i^M w_i \sin(n\phi_i), \quad (4)$$

$$\Psi_n = \frac{1}{n} \tan^{-1} \left(\frac{Q_y}{Q_x} \right), \quad (5)$$

319 where M denotes the number of particles used to determine the event plane, ϕ_i is the azimuthal angle of each particle
 320 and the weight w_i is the charge seen in the corresponding channel of the BBC. Once the event plane is determined,
 321 the elliptic flow v_2 can be extracted by correlating the azimuthal angle of emitted particles ϕ with the event plane:

$$v_2\{\Psi_n\} = \frac{v_2^{\text{obs}}}{\text{Res}\{\Psi_n\}} = \frac{\langle \cos(2[\phi - \Psi_n]) \rangle}{\langle \cos(2[\Psi_n - \Psi_{\text{RP}}]) \rangle}, \quad (6)$$

322 where ϕ is the azimuthal angle of tracks in the laboratory frame, Ψ_n is the n -th order event plane and the brackets
 323 denote an average over all charged tracks and events. The denominator $\text{Res}\{\Psi_n\}$ is the event plane resolution that
 324 corrects for the difference between the estimated event plane Ψ_n and true reaction plane Ψ_{RP} . We measure v_2 using
 325 the same harmonic event plane (Ψ_2) because this leads to a better accuracy [35].

326 The second-harmonic event planes were independently determined with two BBCs located at forward (BBC South)
 327 and backward (BBC North) pseudorapidities $|\eta| = 3.1\text{--}3.9$ [5]. The planes were also combined to provide the event
 328 plane for the full event. More details study on using the BBC for the reaction plane measurement can be found in [24].
 329 The measured v_2 of hadrons in the central arms with respect to the combined second-harmonic BBC event plane will
 330 be denoted throughout this paper as v_2 .

331 1. Event plane determination

332 To determine each event plane we chose the weights at each azimuthal angle to be the charge seen in the corre-
 333 sponding channel of the BBC. Corrections were performed to remove possible biases from small nonuniformities in
 334 the acceptance of the BBC. In this analysis we applied two corrections; the re-centering and shift methods [35]. In the
 335 re-centering method, event flow vectors are shifted and normalized using the mean $\langle Q \rangle$ and width σ of the Q vector
 336 distribution;

$$Q'_x = \frac{Q_x - \langle Q_x \rangle}{\sigma_x}, \quad Q'_y = \frac{Q_y - \langle Q_y \rangle}{\sigma_y}. \quad (7)$$

337 This correction reduces the dependence of the event plane resolution on the laboratory angle. Most acceptance effects
 338 are removed by this re-centering method. The shift method was used as a final correction [35]. In the shift method
 339 the reaction plane is shifted by $\Delta\Psi_n$ defined by

$$n\Delta\Psi_n(\Psi_n) = \sum_{k=1}^{k_{\text{max}}} \frac{2}{k} [-\langle \sin(kn\Psi_n) \rangle \cos(kn\Psi_n) + \langle \cos(kn\Psi_n) \rangle \sin(kn\Psi_n)], \quad (8)$$

340 where $k_{\text{max}} = 8$ in this analysis. The shift ensures that $dN/d\Psi_n$ is isotropic. When k_{max} was reduced to $k_{\text{max}} = 4$,
 341 the difference in the extracted v_2 was negligible and thus we include no systematic uncertainty due to the choice of
 342 k_{max} in our v_2 results [24].

343 Independent re-centering and shift corrections were applied to each centrality selection, in 5% increments, as well
 344 as 20 cm steps in z -vertex. This optimizes the event plane resolution. The corrections were also performed for each
 345 experimental run (the duration of a run is typically 1-3 hours) to minimize the possible time-dependent response of
 346 detectors.

347 2. Event plane resolution

348 The event plane resolution for v_2 was evaluated by the two-subevent method. The event plane resolution [35] is
 349 expressed as

$$\begin{aligned} \langle \cos(kn[\Psi_n - \Psi_{\text{RP}}]) \rangle &= \frac{\sqrt{\pi}}{2\sqrt{2}} \chi_n e^{-\chi_n^2/4} \\ &\times \left[I_{(k-1)/2} \left(\frac{\chi_n^2}{4} \right) + I_{(k+1)/2} \left(\frac{\chi_n^2}{4} \right) \right], \end{aligned} \quad (9)$$

350 where $\chi_n = v_n \sqrt{2M}$, M is the number of particles used to determine the event plane Ψ_n , I_k is the modified Bessel
 351 function of the first kind and $k = 1$ for the second harmonic BBC event plane.

352 To determine the event plane resolution we need to determine χ_n . Because the North and South BBCs have
 353 approximately the same η coverage, the event plane resolution of each sub-detector is expected to be the same. Thus,
 354 the subevent resolution for south and north event planes can be expressed as

$$\langle \cos(2[\Psi_n^{\text{S(N)}} - \Psi_{\text{RP}}]) \rangle = \sqrt{\langle \cos(2[\Psi_n^{\text{S}} - \Psi_n^{\text{N}}]) \rangle}, \quad (10)$$

355 where $\Psi_n^{\text{S(N)}}$ denotes the event plane determined by the South (North) BBC. Once the subevent resolution is obtained
 356 from Eq. (10), one can calculate χ_n^{sub} using Eq. (9). The χ_n for the full event can then be estimated by $\chi_n = \sqrt{2}\chi_n^{\text{sub}}$.
 357 This is then substituted into Eq. (9) to give the full event resolution. Because the multiplicity of the full event is
 358 twice as large as that of the subevent, χ_n is proportional to \sqrt{M} .

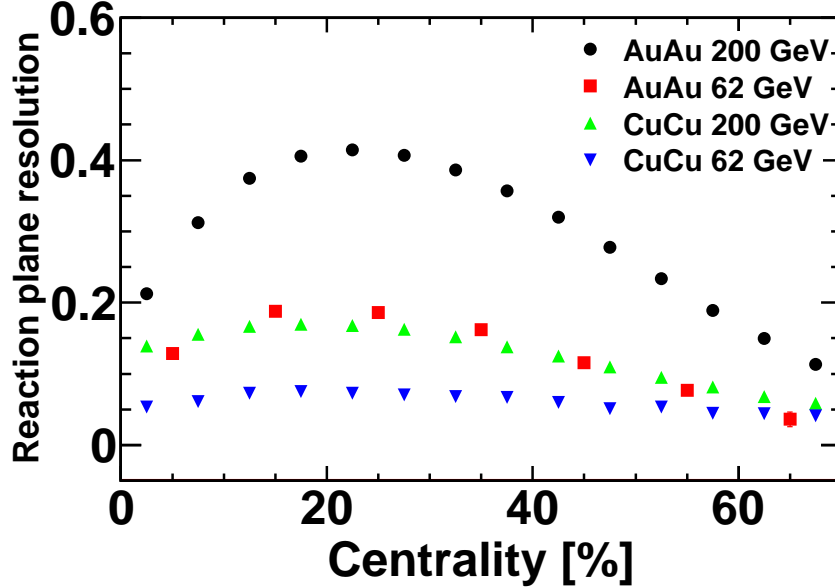


FIG. 4. (Color online) Second-order event plane resolution vs. centrality in Au+Au and Cu+Cu at 200 and 62.4 GeV. The event plane is measured by BBC.

359 Figure 4 shows the BBC North-South-combined resolution of the event plane as a function of the centrality in
 360 Au+Au and Cu+Cu at $\sqrt{s_{NN}} = 200$ and 62.4 GeV. The reaction-plane resolution and its uncertainties in Au+Au
 361 and Cu+Cu at 62.4 and 200 GeV are summarized in Table III.

362 E. Systematic uncertainty for v_2

363 The sources of systematic uncertainty on the v_2 measurement include: reaction plane determination, the effects of
 364 matching cuts, the effects of the E/p cut, and occupancy effects for PID v_2 . These are described below.

365 The systematic uncertainties due to the reaction plane determination were estimated by comparing the v_2 values ex-
 366 tracted using three different reaction planes; the BBC North, BBC South, and BBC North-South combined. Figure 5a

TABLE III. Reaction-plane resolution for each centrality in Au+Au and Cu+Cu collisions at $\sqrt{s_{NN}} = 200$ and 62.4 GeV and its statistical contribution to the uncertainty on v_2 . Note: Centrality bins are 10% wide (0%–10%, 10%–20%, etc.) for Au+Au 62.4 GeV.

Centrality bin	Au+Au 200 GeV		Au+Au 62.4 GeV		Cu+Cu 200 GeV		Cu+Cu 62.4 GeV	
	Resolution	Stat. Uncert. for v_2 [%]	Resolution	Stat. Uncert. for v_2 [%]	Resolution	Stat. Uncert. for v_2 [%]	Resolution	Stat. Uncert. for v_2 [%]
0%–5%	0.212	0.20	0.128	2.0	0.139	0.55	0.053	5.6
5%–10%	0.312	0.09			0.155	0.44	0.061	4.3
10%–15%	0.375	0.06	0.189	0.94	0.167	0.38	0.073	3.0
15%–20%	0.405	0.05			0.170	0.37	0.075	2.8
20%–25%	0.414	0.05	0.186	0.97	0.168	0.38	0.073	3.0
25%–30%	0.407	0.05			0.162	0.40	0.071	3.2
30%–35%	0.387	0.06	0.163	1.3	0.152	0.46	0.068	3.4
35%–40%	0.357	0.07			0.138	0.56	0.067	3.5
40%–45%	0.320	0.09	0.118	2.4	0.125	0.68	0.060	4.4
45%–50%	0.278	0.12			0.110	0.88	0.051	6.1
50%–55%	0.234	0.16	0.079	5.4	0.095	1.2	0.054	5.6
55%–60%	0.189	0.25			0.082	1.6	0.045	7.9
60%–65%	0.150	0.40	0.044	17.5	0.068	2.3	0.044	8.2
65%–70%	0.113	0.70			0.058	3.1	0.041	9.6

TABLE IV. Systematic uncertainty [%] of the reaction plane determination for each data set and each centrality bin. These are obtained by taking the larger values away from unity of the ratio of v_2 with BBC North and South to v_2 with BBC North-South-combined.

Centrality bin	Au+Au		Cu+Cu	
	200 GeV	62.4 GeV	200 GeV	64 GeV
0%–10%	2	3	3	14
10%–20%	3	2	2	9
20%–30%	4	2	2	6
30%–40%	4	7	2	2
40%–50%	3	7	2	3
50%–60%	3	5	2	5

367 shows v_2 vs. centrality for three reaction planes (BBC South, North, South-North combined) for Au+Au 200 GeV.
 368 The bottom panel shows the ratio of v_2 with BBC North and South RP to v_2 with BBC North-South combined
 369 (default). The percentage systematic uncertainty was obtained by taking the largest values away from unity of these
 370 ratios. These uncertainties are summarized in Table IV summarizes for each data set and each centrality bin.

TABLE V. Systematic uncertainty [%] of the matching and E/p cuts for each data set and each p_T bin for minimum bias event sample, which are obtained by taking the larger values of the ratio of v_2 with different matching cut to v_2 with the default matching cut.

p_T (GeV/c)	Au+Au 200 GeV		Au+Au 62.4 GeV		Cu+Cu 200 GeV		Cu+Cu 62.4 GeV	
	Systematic Uncertainty (%)		Systematic Uncertainty (%)		Systematic Uncertainty (%)		Systematic Uncertainty (%)	
	Matching cut	E/p cut	Matching cut	E/p cut	Matching cut	E/p cut	Matching cut	E/p cut
0.2–1.0	1	1	1	2	1	3	2	3
1.0–2.0	1	3	1	4	1	2	1	2
2.0–4.0	1	2	4	3	1	3	2	3

371 The default matching cuts for tracks projected to PC3 are $-2.5\sigma < (d\phi_{PC3} \text{ and } dz_{PC3}) < 2.5\sigma$. To obtain
 372 the systematic uncertainty from the dependence on these matching cuts, we examined different cut windows, e.g.
 373 $|d\phi_{PC3}| < 1.0\sigma$ and $1.0\sigma < |d\phi_{PC3}| < 2.5\sigma$, and compared v_2 values using these cuts to v_2 values from the default
 374 cut. The difference between v_2 values with these matching cuts determine the systematic uncertainties. Because the
 375 alternative cut windows have a smaller sample of data, we extracted the systematic uncertainty from the minimum
 376 bias event sample and used these for all centralities. Table V shows the matching systematic uncertainties.

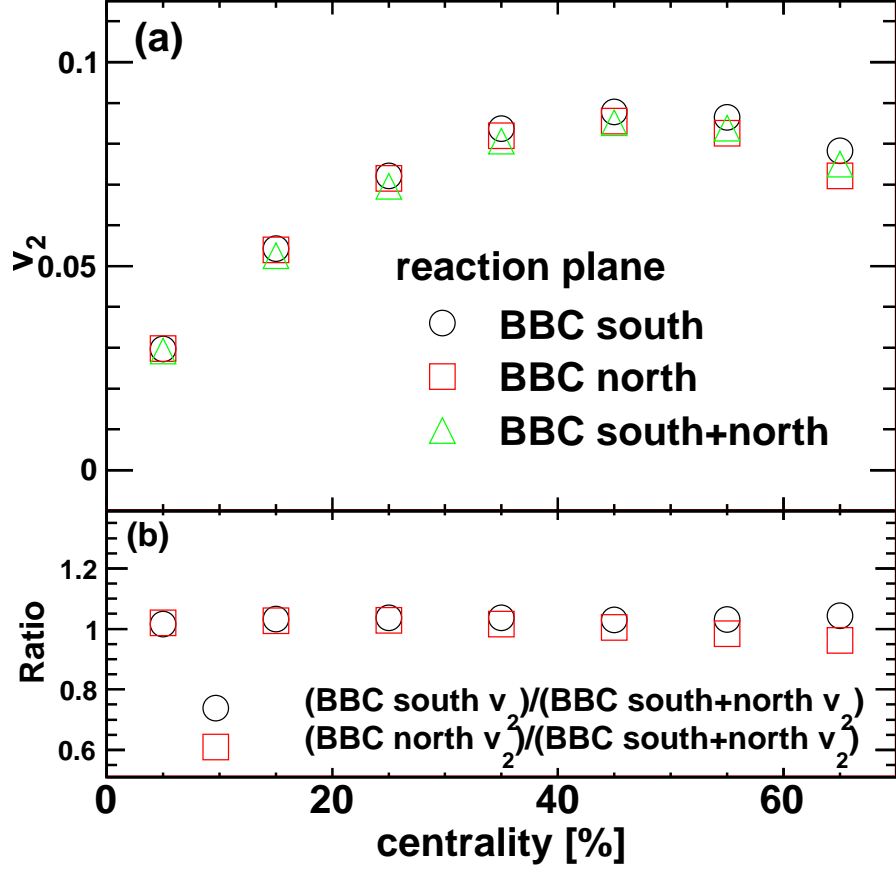


FIG. 5. (Color online) (a) v_2 vs. centrality with three different reaction planes (BBC South, North, South-North combined) for Au+Au 200 GeV. (b) The ratio of v_2 with BBC South or North reaction plane to v_2 with South-North combined.

377 The E/p cut can reject background from conversions, especially for high p_T tracks. The default cut, $E/p > 0.2$, was
 378 used for tracks with $p_T > 4$ GeV/ c . To test the sensitivity to the value of the cut, we apply cuts of $E/p > 0.1$, 0.2 and
 379 0.3 cuts for tracks $3 < p_T < 4$ GeV/ c ; a lower momentum was used because we have more statistics there. The ratio
 380 of v_2 with different E/p cuts contributes to the systematic uncertainty. We obtained the systematic uncertainty due
 381 to the E/p cut using the minimum bias event sample, because within the statistics we did not observe any centrality
 382 dependence for how v_2 changed with different E/p cuts. Table V lists the systematic uncertainties from the E/p cut.
 383 Both EMCAL and TOF detectors are used for particle identification. In the low p_T region both detectors can be
 384 used, and the difference between v_2 measured with the EMCAL and TOF, averaged across p_T , is used for the systematic
 385 uncertainty due to timing performance. This includes the 1% uncertainty due to background contributions in the
 386 particle identification. The values are summarized in Table VI. Note, that the timing systematic uncertainty only
 387 affects the identified hadron results.

TABLE VI. Systematic uncertainty [%] for v_2 of identified hadrons due to the timing performance of the EMCAL and TOF detectors. These are obtained by taking the difference between v_2 with EMCAL and v_2 with TOF merging p_T and centrality bins.

Collision Species	$\sqrt{s_{NN}}$ [GeV]	identified hadron		
		π	K	p
Au+Au	62.4	2	4	6
Cu+Cu	200	3	5	6

388 The values for v_2 can be impacted due to finite occupancy which tends to lower the measured v_2 . The magnitude

of this effect has been estimated to be largest for central Au+Au collisions at 200 GeV as a reduction in v_2 for PID particles of approximately 0.0013 for the running conditions of the data presented here. This effect is independent of p_T . For different centrality and beam-energies we take the systematic uncertainty on PID v_2 to linearly decrease with the average charged particle multiplicity in those collisions.

IV. RESULTS FOR V_2 OF INCLUSIVE CHARGED HADRONS

In this section we describe the v_2 measurements and how they change as a function of collision energy and system size. We present the measured v_2 for inclusive charged particles in Au+Au and Cu+Cu collisions at 62.4 and 200 GeV. For 200 GeV, the v_2 results for $p_T < 5$ GeV/ c are obtained by re-binning the data published in [7, 24, 36]. The new 200 GeV data published in this paper are v_2 results for $p_T > 5$ GeV/ c . In addition the 62.4 GeV Cu+Cu data are new results original in this paper.

The centrality selections of each collision system are:

1. Au+Au collisions at $\sqrt{s_{NN}} = 200$ GeV
 - Minimum Bias ; 0%–92%
 - 10% steps ; 0%–10%, 10%–20%, 20%–30%, 30%–40%, 40%–50%, 50%–60%
 - 20% steps ; 0%–20%, 20%–40%, 40%–60%
 - Most peripheral bin ; 60%–92%
2. Au+Au collisions at $\sqrt{s_{NN}} = 62.4$ GeV
 - Minimum Bias ; 0%–83%
 - 10% steps ; 0%–10%, 10%–20%, 20%–30%, 30%–40%, 40%–50%
3. Cu+Cu collisions at $\sqrt{s_{NN}} = 62.4$ and 200 GeV
 - Minimum Bias ; 0%–88%
 - 10% steps ; 0%–10%, 10%–20%, 20%–30%, 30%–40%, 40%–50%

A. v_2 vs. p_T results for inclusive charged hadrons

1. Au+Au at $\sqrt{s_{NN}} = 200$ GeV

We analyzed 860 million Au+Au collisions at 200 GeV collected during the 2003-04 experimental period, which is more than 20 times larger than the sample of events (30 M) analyzed from the 2001-02 experimental period [5]. Figure 6 shows the v_2 for inclusive charged hadrons in Au+Au collisions at 200 GeV.

2. Au+Au at $\sqrt{s_{NN}} = 62.4$ GeV

For Au+Au collisions at 62.4 GeV, 30 million events were analyzed to study the dependence of v_2 on collision center-of-mass energy. The measured v_2 results from this collision system are shown in Fig. 7, together with the results from Au+Au 200 GeV collisions. The values of N_{part} are very similar at these two beam energies. We observe that the v_2 measurements for Au+Au collisions at 62.4 GeV are consistent with those for Au+Au at 200 GeV, within the combined statistical and systematic uncertainties.

3. Cu+Cu at $\sqrt{s_{NN}} = 200$ and 62.4 GeV

For Cu+Cu collisions at 62.4 GeV, 340 million events were analyzed to study the dependence of v_2 on collision center-of-mass energy and system size. Figure 8 shows the v_2 results at 62.4 GeV in minimum bias events and 10% centrality selections. These are compared with Cu+Cu 200 GeV v_2 results [7]. The v_2 results for Cu+Cu collisions at 62.4 GeV are clearly smaller than those in 200 GeV collisions, especially at $p_T < 1.5$ GeV/ c .

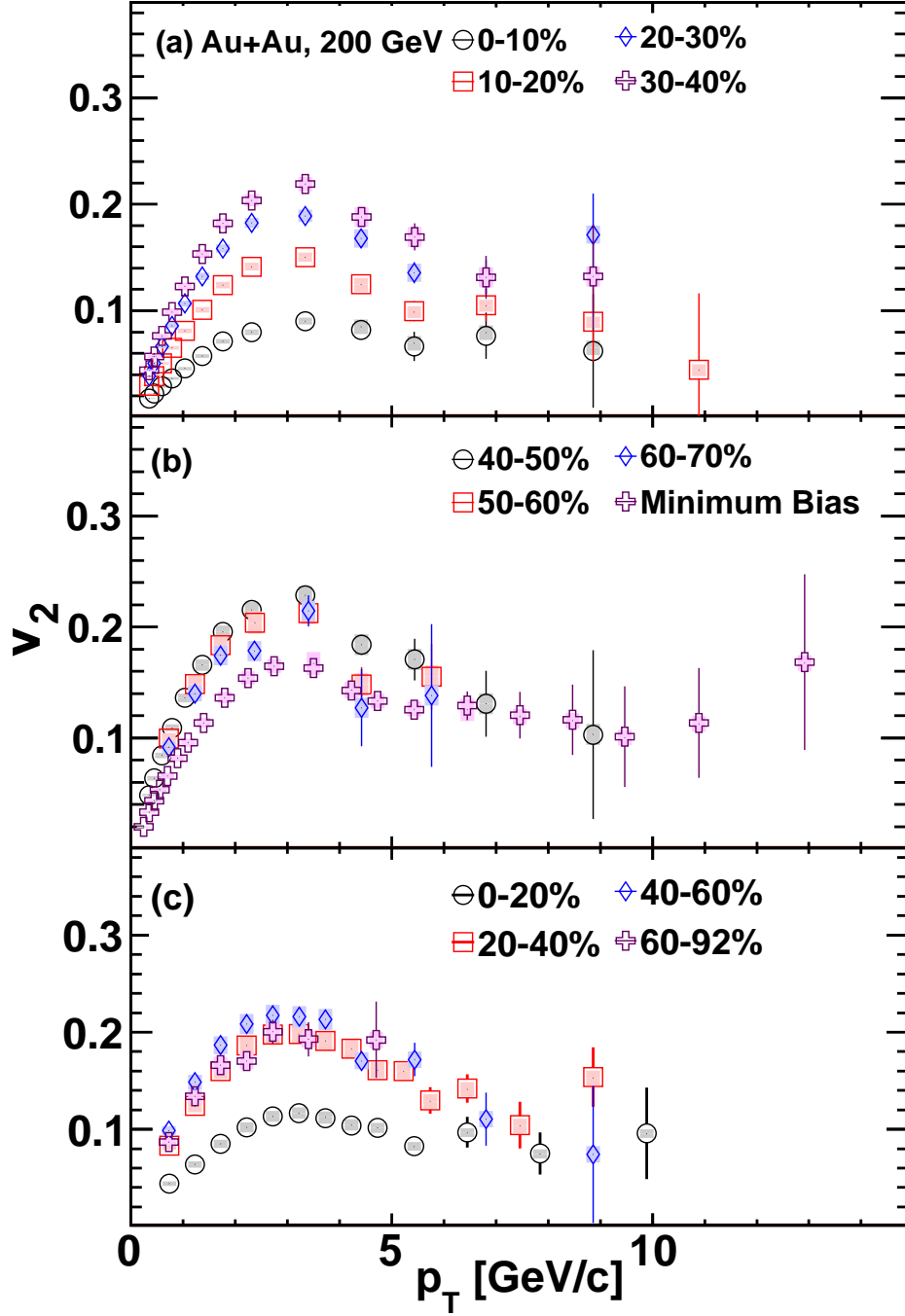


FIG. 6. (Color online) v_2 for inclusive charged hadrons in Au+Au at $\sqrt{s_{NN}}=200$ GeV for the centralities indicated. The error bars show statistical uncertainties and the bands show systematic uncertainties. In many cases, the systematic uncertainties are smaller than the symbols.

427

B. System comparisons

428

1. Centrality and collision energy dependence

429 An alternative view of these data is to make separate p_T selections and to plot v_2 in a given p_T range as a function
 430 of centrality and collision energy. Figure 9 presents the Au+Au data as a function of centrality, where triangles,
 431 boxes, and circles correspond to three p_T bins: 0.2–1.0, 1.0–2.0 and 2.0–4.0 GeV/c respectively. The two different

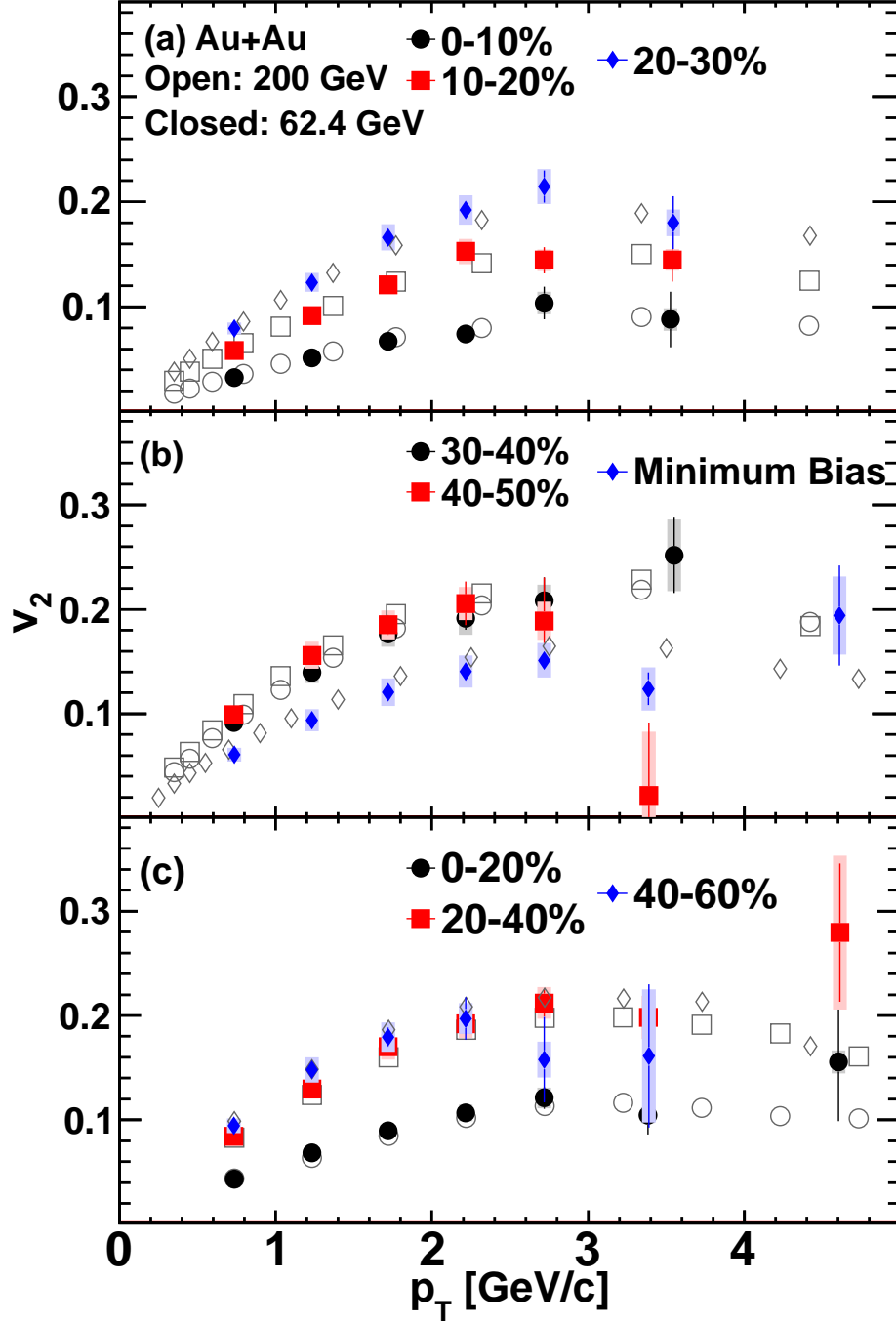


FIG. 7. (Color online) v_2 for inclusive charged hadrons in Au+Au at $\sqrt{s_{NN}} = 62.4$ and 200 GeV for the centralities indicated. The error bars show statistical uncertainties and the bands show systematic uncertainties. In many cases, the systematic uncertainties are smaller than the symbols.

432 beam energies are presented by open and closed symbols for 62.4 and 200 GeV respectively. The data confirms prior
 433 results that v_2 increases from central to midcentral collisions and then begins to decrease again towards peripheral
 434 collisions. The v_2 for Au+Au at 62.4 and 200 GeV agree to within statistical and systematic uncertainties for all
 435 measured centralities.

436 A similar v_2 comparison has been carried out by the STAR experiment reaching even lower energies from $\sqrt{s_{NN}}$
 437 = 7.7 to 200 GeV [19]. Their results show that the $v_2(p_T)$ increases slightly from 7.7 up to 39 GeV, then saturates
 438 above 39 GeV.

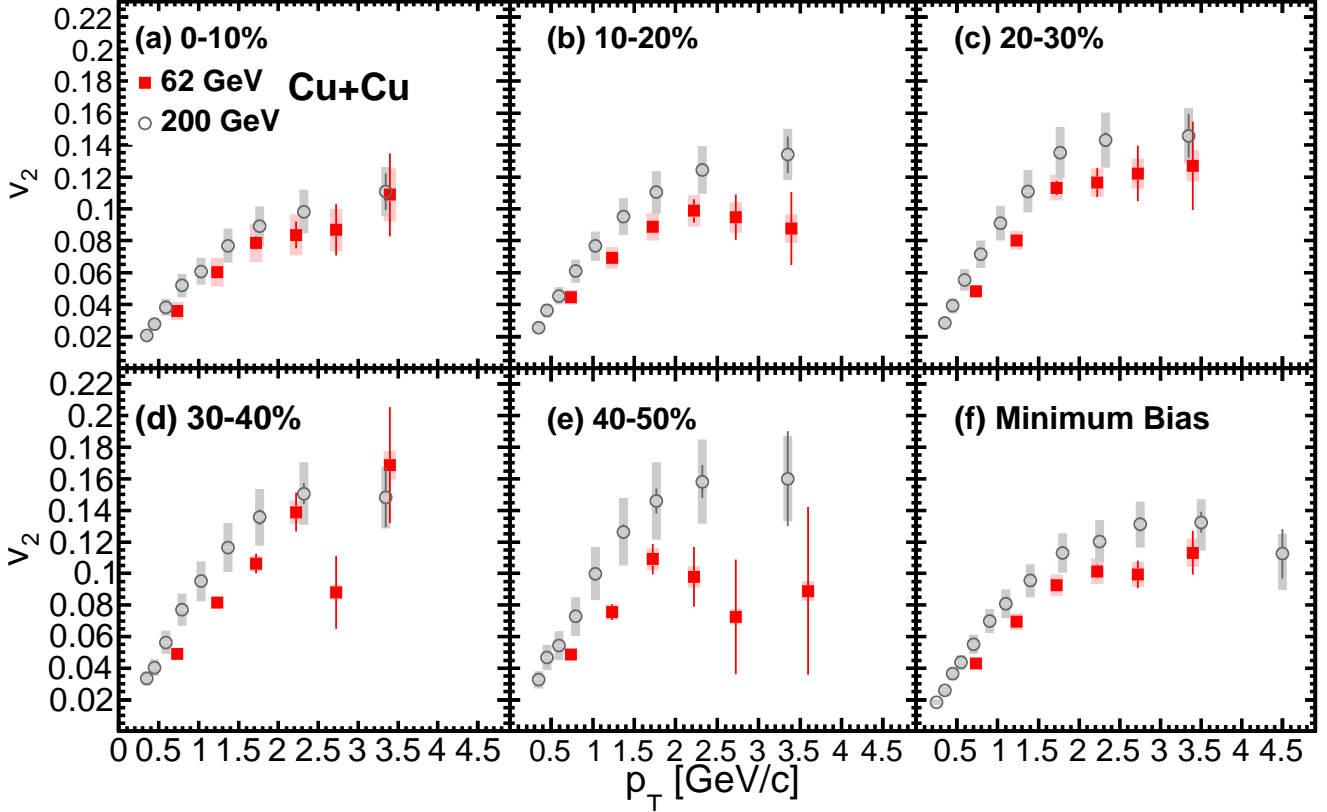


FIG. 8. (Color online) v_2 for inclusive charged hadrons in Cu+Cu at $\sqrt{s_{NN}} = 62.4$ GeV compared with 200 GeV [7] for the centralities indicated. The error bars show statistical uncertainties and the bands show systematic uncertainties. In many cases, the systematic uncertainties are smaller than the symbols.

439 Figure 10 shows the centrality dependence of v_2 for charged hadrons emitted at different p_T from Cu+Cu collisions
 440 at 62.4 and 200 GeV. The statistical uncertainties are larger due to lower statistics for the Cu+Cu in the 62.4 GeV
 441 data sample. The measured v_2 values are lower at 62.4 GeV compared with 200 GeV.

442 We have made a comparison between the measured PHENIX v_2 and the previously published STAR v_2 measure-
 443 ment [20] in Cu+Cu collisions and found them to be generally consistent. For 200 GeV Cu+Cu the PHENIX v_2
 444 are higher by about 10% in the 0-10%, 10-20%, 20-30% and 30-40% centrality bins, and higher by about 20% in
 445 40-50% bin; these differences are within statistical and systematic uncertainties of the PHENIX results in all cases.
 446 At 62.4 GeV the PHENIX v_2 is lower by approximately 10% in the 0-40% bins and by 20% in 40-50% bin. These
 447 differences are within statistical and systematic uncertainties in the 0-20% bins, though they are roughly twice the
 448 statistical and systematic uncertainties in 20-50% bins, taking into account errors on the PHENIX measurement alone.

449 2. Geometry dependence, eccentricity and N_{part}

450 There are two ways to establish the extent that v_2 changes with the system size: one is to change the collision
 451 centrality, the other is to change the colliding nuclei. As seen in Fig. 11, the measured v_2 in Cu+Cu collisions is
 452 smaller than that of Au+Au at a comparable N_{part} .

453 Because ε is different between Au+Au and Cu+Cu collisions at the same N_{part} , we can try to normalize v_2 by ε .
 454 In the lower row of Fig. 11, v_2 normalized by ε is similar in magnitude for both Cu+Cu and Au+Au collisions. This
 455 confirms that the eccentricity normalization can account for the effect of the initial geometrical anisotropy [30]. The
 456 exception is that the Cu+Cu 62.4 GeV data falls below the other data. Note that the ratio v_2/ε also depends on
 457 centrality (N_{part}) and that there is a similar rate of increase of v_2/ε with N_{part} for all three p_T bins: 0.2–1.0, 1.0–2.0,
 458 and 2.0–4.0 GeV/c. This pattern suggests the need for an additional normalization or scaling factor that depends on
 459 N_{part} .

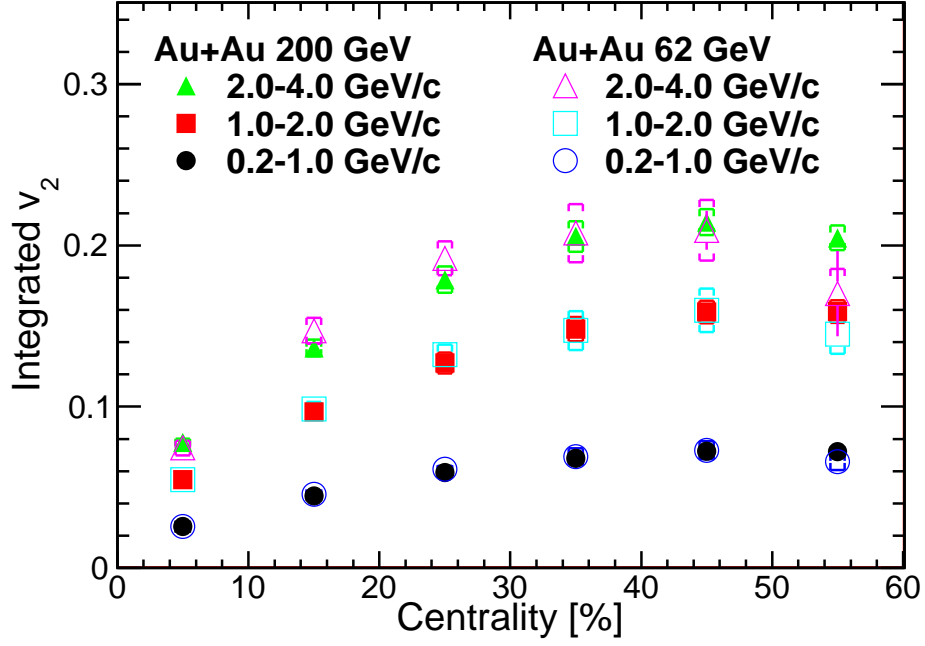


FIG. 9. (Color online) Comparison of integrated v_2 at $\sqrt{s_{NN}} = 62.4$ and 200 GeV in Au+Au. Solid symbols indicate $\sqrt{s_{NN}} = 200$ GeV and open symbols indicate $\sqrt{s_{NN}} = 62.4$ GeV. Ranges of p_T integrated are 0.2–1.0 (circles), 1.0–2.0 (squares), and 2.0–4.0 (triangles) GeV/ c . The bars indicate the statistical uncertainties and the boxes indicate the systematic uncertainties. In many cases, the systematic uncertainties are smaller than the symbols.

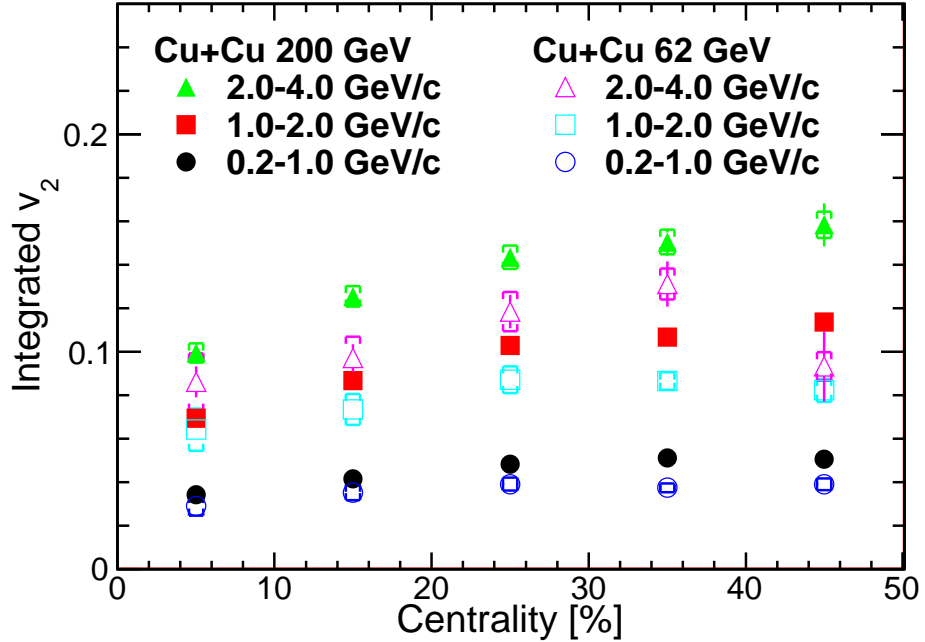


FIG. 10. (Color online) Comparison of integrated v_2 at $\sqrt{s_{NN}} = 62.4$ and 200 GeV in Cu+Cu. Open symbols indicate $\sqrt{s_{NN}} = 62.4$ GeV and filled symbols indicate $\sqrt{s_{NN}} = 200$ GeV. Ranges of p_T integrated are 0.2–1.0 (circles), 1.0–2.0 (squares), and 2.0–4.0 (triangles) GeV/ c . The bars indicate the statistical uncertainties and the boxes indicate the systematic uncertainties. In many cases, the systematic uncertainties are smaller than the symbols.

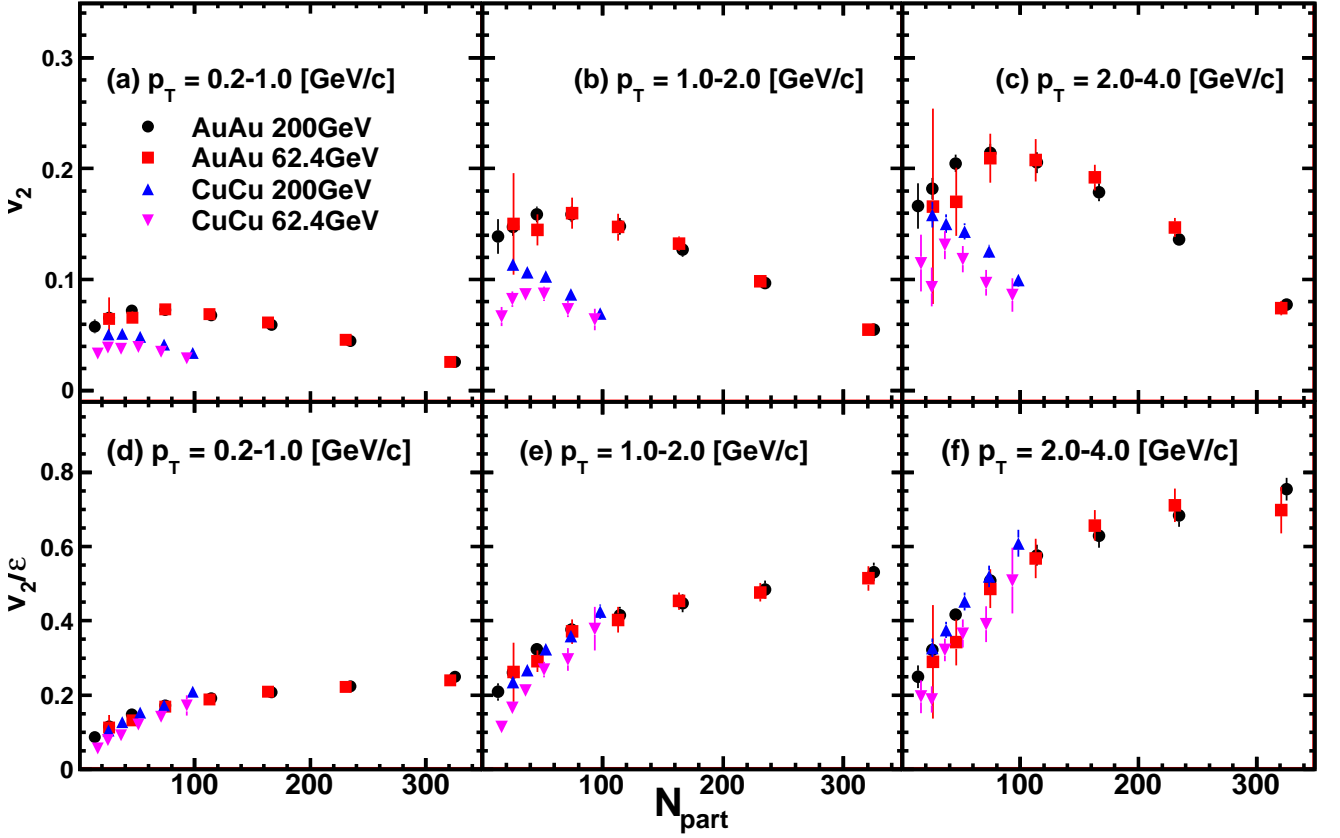


FIG. 11. (Color online) The top three panels show the comparison of integrated v_2 as a function of N_{part} and the bottom three panels show the comparison of the normalized v_2/ε vs. N_{part} in both Au+Au and Cu+Cu at 200 GeV and 62.4 GeV. The ranges of p_T integration are 0.2–1.0, 1.0–2.0 and 2.0–4.0 GeV/c from left to right and top to bottom panels respectively. Both statistical and systematic uncertainties are included in the error bars.

460 Figure 12 is a comparison of v_2 as a function of p_T for centrality classes that have approximately the same value
 461 of ε but with different values of N_{part} . The average N_{part} is 166.6 for 20%–30%, 114.2 for 30%–40% and 45.5 for
 462 50%–60% in Au+Au collisions, while N_{part} is 73.6 for 10%–20%, 53.0 for 20%–30% and 25.4 for 40%–50% in Cu+Cu
 463 collisions. It can be clearly seen that v_2 increases with N_{part} for similar ε .

464 3. Participant $N_{\text{part}}^{1/3}$ scaling

465 We empirically explore using $N_{\text{part}}^{1/3}$ as a potential scaling factor of v_2 in addition to ε . We draw on results with a
 466 different observable, namely that the HBT source sizes at RHIC have been observed to scale with $N_{\text{part}}^{1/3}$ [37]. Under
 467 the phenomenological assumption that N_{part} is proportional to the volume of hot/dense matter formed in high-energy
 468 nuclear collisions, $N_{\text{part}}^{1/3}$ can be considered as a quantity proportional to a length scale.

469 Figure 13 plots $v_2/(\varepsilon \cdot N_{\text{part}}^{1/3})$ for integrated bins of $p_T = 0.2$ –1.0, 1.0–2.0, and 2.0–4.0 GeV/c. This combination of
 470 two scaling factors works well, i.e. the scaled data are at comparable values, with the exception of the Cu+Cu data
 471 at 62.4 GeV which deviate from this scaling, particularly at $N_{\text{part}} \leq 40$. That this empirical $v_2/(\varepsilon \cdot N_{\text{part}}^{1/3})$ scaling
 472 works well suggests that v_2 is determined by both the initial geometrical anisotropy and the number of participants.

473 Other scalings for the system size dependence have been suggested, particularly $1/S_{xy}dN/dy$ [38] where S_{xy} is the
 474 transverse area of the participant zone. Because dN/dy is proportional to N_{part} at a given beam energy and S_{xy} is
 475 approximately proportional to $(N_{\text{part}})^{2/3}$, $1/S_{xy}dN/dy$ is then proportional to $N_{\text{part}}^{1/3}$.

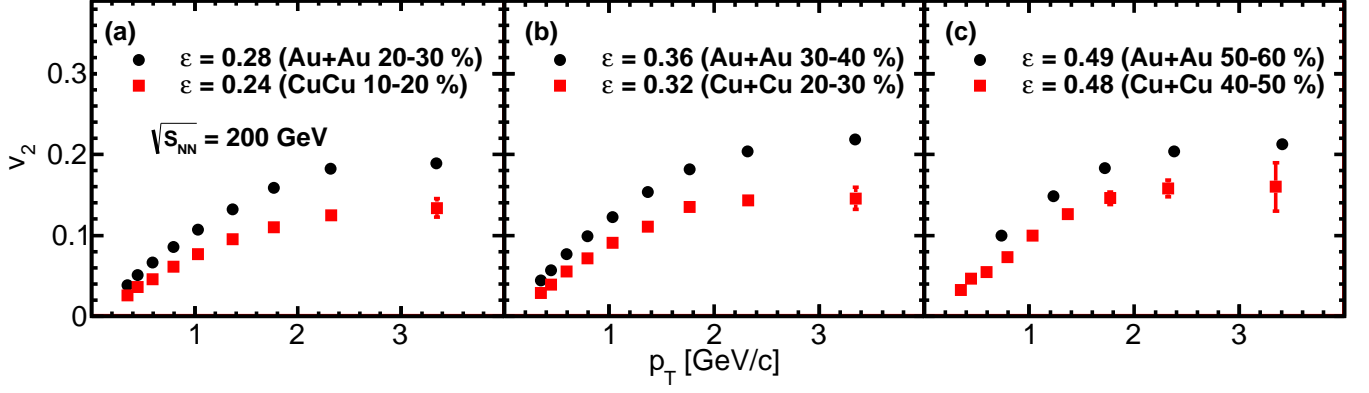


FIG. 12. (Color online) Comparison of $v_2(p_T)$ at 200 GeV for two example systems with different collision size (Au+Au or Cu+Cu) but approximately the same ϵ . Black symbols indicate Au+Au and red symbols indicate Cu+Cu. The average number of participants N_{part} is 166.6 for 20%–30%, 114.2 for 30%–40% and 45.5 for 50%–60% at Au+Au collisions, and N_{part} is 73.6 for 10%–20%, 53.0 for 20%–30% and 25.4 for 40%–50% at Cu+Cu collisions.

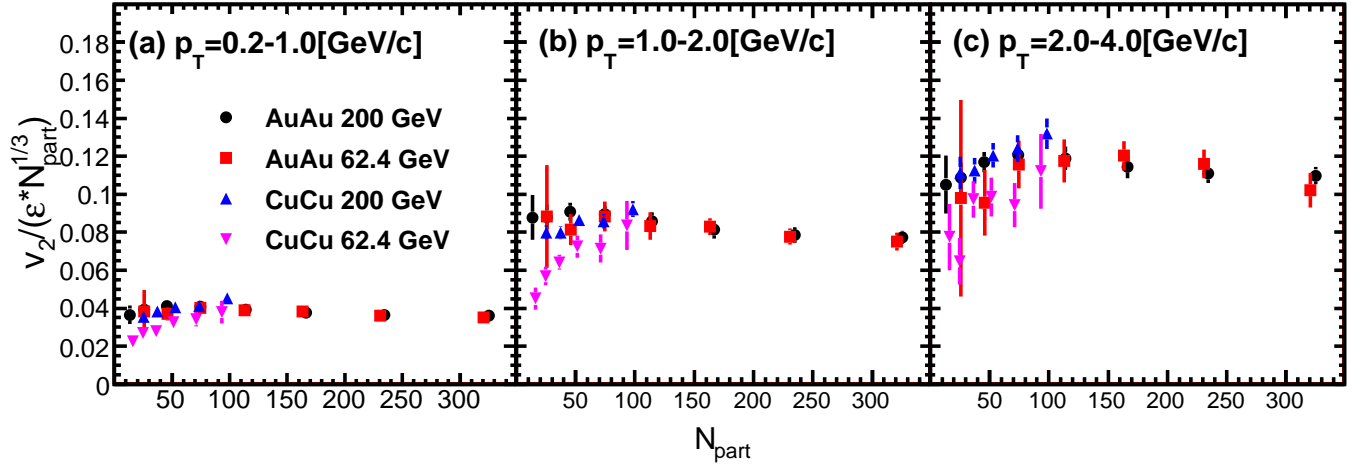


FIG. 13. (Color online) Comparison of integrated $v_2/(\epsilon \cdot N_{\text{part}}^{1/3})$ as a function of N_{part} for two collision energies and two collision systems, Au+Au at 200 GeV, Au+Au at 62.4 GeV, Cu+Cu at 200 GeV and Cu+Cu at 62.4 GeV. Ranges of p_T integration are 0.2–1.0, 1.0–2.0 and 2.0–4.0 GeV/c from left to right panels respectively. All uncertainties from the measured v_2 , ϵ , and N_{part} are included in the error bars.

476

V. RESULTS FOR V_2 OF IDENTIFIED CHARGED HADRONS

477 More information can be obtained by examining v_2 for charged pions, kaons and (anti) protons ($\pi/K/p$) each as
 478 a function of transverse momentum p_T . The charged particles are identified by TOF and EMCAL and the data are
 479 presented for several classes of collision centrality;

- 480 1. Au+Au collisions at $\sqrt{s_{NN}} = 62.4$ GeV
 - 481 • 10%–40% (Particles and antiparticles are measured separately.)
 - 482 • 10% bins from 0% to 50% (Particles and antiparticles are measured together.)
- 483 2. Au+Au collisions at $\sqrt{s_{NN}} = 200$ GeV
 - 484 • 0%–92% (Particles and antiparticles are measured separately.)
 - 485 • 10% bins from 0% to 50% (Particles and antiparticles are measured together.)
- 486 3. Cu+Cu collisions at $\sqrt{s_{NN}} = 200$ GeV

487

- 10% bins from 0% to 50% (Particles and antiparticles are measured together.)

488 Note we do not present Cu+Cu 62.4 GeV data in this section because there were insufficient statistics to determine
489 v_2 for identified particles.

490

A. Beam energy dependence

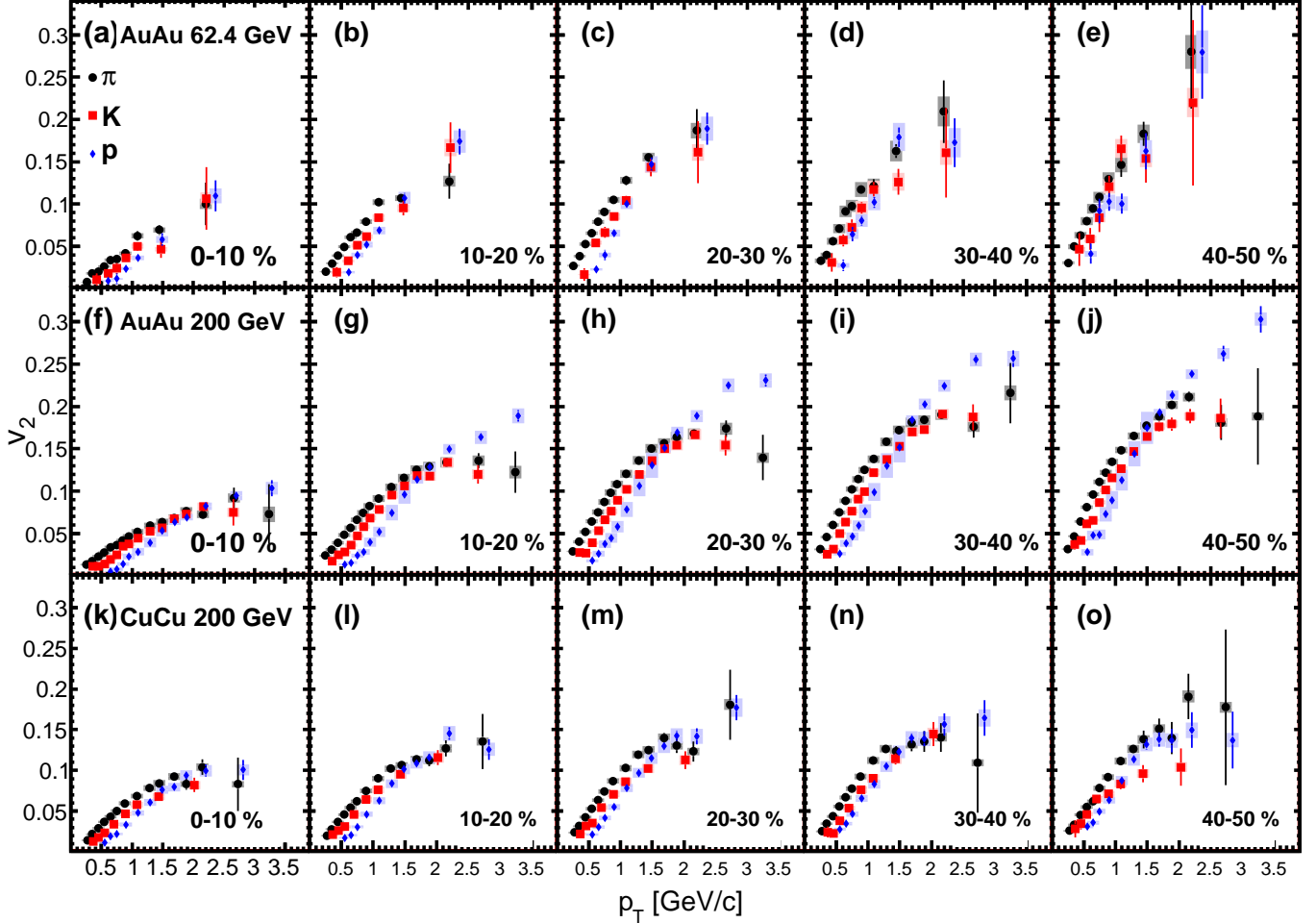


FIG. 14. (Color online) v_2 vs. p_T for $\pi/K/p$ emitted from Au+Au at 62.4 and 200 GeV and Cu+Cu at 200 GeV collisions for the centralities indicated. The lines for each point indicate the statistical uncertainties, and the boxes are systematic uncertainties. In many cases, the systematic uncertainties are smaller than the symbols.

491 Figure 14 shows a summary of v_2 measurements of identified particles $\pi/K/p$ for three different data sets; Au+Au
492 at 62.4 and 200 GeV and Cu+Cu at 200 GeV. Figure 15 shows the comparison between 62.4 and 200 GeV for Au+Au
493 collisions. The measured v_2 in the 62.4 and 200 GeV data sets are consistent, within the systematic uncertainties,
494 with the exception of proton v_2 at 62.4 GeV which is slightly higher than at 200 GeV in the lower p_T region. These
495 small differences could be caused by larger radial flow at higher $\sqrt{s_{NN}}$, especially for heavier particles such as protons.

496 The observation that the proton v_2 is larger at 62.4 GeV than at 200 GeV for Au+Au collisions is opposite to
497 the earlier observation that inclusive charged v_2 at 62.4 GeV is lower than that at 200 GeV Cu+Cu. Therefore, the
498 differences in lower v_2 for inclusive charged hadrons from Cu+Cu may be caused by different physics than the radial
499 flow effect seen in Au+Au collisions.

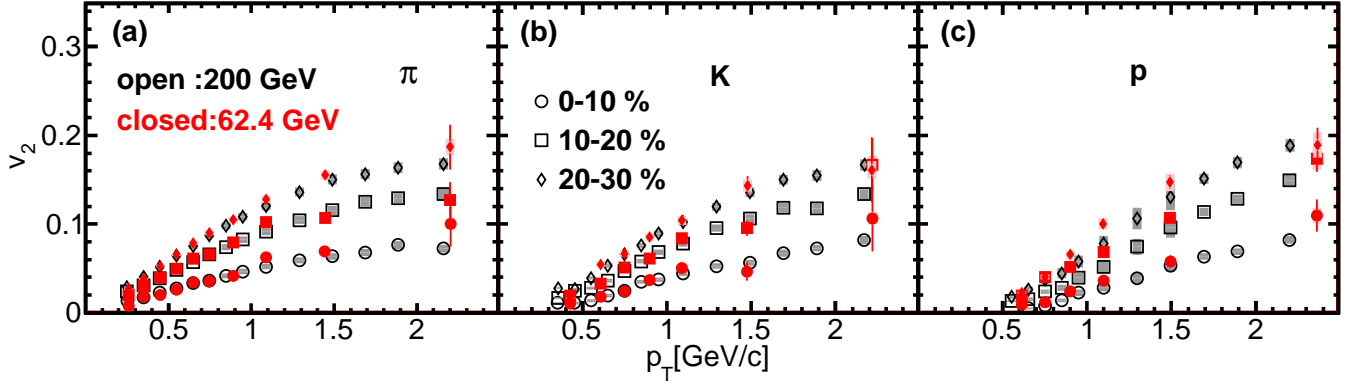


FIG. 15. (Color online) Comparison of v_2 between $\sqrt{s_{NN}} = 62.4$ and 200 GeV for $\pi/K/p$ emitted from 0%–10%, 10%–20% and 20%–30% central Au+Au collisions. Both results for all species agree within the errors. The lines indicate the statistical uncertainties at each point and the boxes indicate the systematic uncertainties. In many cases, the systematic uncertainties are smaller than the symbols.

500

B. Particle-antiparticle comparison

When we examine identified v_2 we will combine opposite charged particles, e.g. π^\pm , to form πv_2 . Prior results on the ratio of v_2 for antiparticles and particles can be found in Refs. [19, 39]. In this section we compare the particle and antiparticle v_2 in Au+Au collisions at 200 and 62.4 GeV in wide centrality classes: a minimum bias sample (0%–92%) for 200 GeV and 10%–40% for 62.4 GeV data. The first and second rows of plots in Fig. 16 present v_2 as a function of p_T for π^\pm , K^\pm , p and \bar{p} in Au+Au collisions at 200 and 62.4 GeV. The lines for each point are the statistical uncertainties and the boxes are systematic uncertainties.

At both 200 and 62.4 GeV, the the measured Au+Au v_2 values of particle and antiparticle are comparable to each other within uncertainty, though there is a possible indication of a small reduction of anti-proton v_2 at lower p_T . When we combine particle and anti-particle v_2 we average over these differences.

510

C. Number of valence quark n_q scaling of v_2

The v_2 measurements of identified particles $\pi/K/p$ for three different data sets; Au+Au at 62.4 and 200 GeV and Cu+Cu at 200 GeV collisions are re-plotted in Fig. 17 after scaling by the number of constituent quarks for both v_2 and p_T axes as shown. An alternative scaling is to use transverse kinetic energy. We define transverse kinetic energy as $KE_T = m_T - m$, where m is the mass of the hadron and $m_T = \sqrt{p_T^2 + m^2}$. The quark number scaled v_2 are shown as a function of KE_T/n_q for all three data sets in Fig. 18.

Note that at higher values, $KE_T/n_q > 0.7$, PHENIX has observed significant deviations from n_q scaling for Au+Au noncentral collisions[8]. Those higher KE_T results indicate that the azimuthal anisotropy of these high KE_T particles are impacted by mechanisms such as parton-energy loss, jet chemistry, and/or different fragmentation functions. For comparison, at the LHC [17, 18], v_2 does not scale well with the quark number and transverse kinetic energy of the hadron in any range of KE_T/n_q , with up to 40% deviations observed at low values of KE_T/n_q .

To quantify how well the number of quark scaling with KE_T works with the current data, we fit all the hadron species data in Figure 18 with a common polynomial function for each centrality and colliding system. We divide the data by these fits to compare how close different hadron species are to the common scaled shape of v_2 . Figure 19 shows these ratios as a function of KE_T/n_q for $\pi/K/p$ in Au+Au and Cu+Cu. Deviations from the fitted polynomial function are observed, especially with the high statistics data sets at 200 GeV Au+Au and 200 GeV Cu+Cu collisions. For Au+Au central collisions in the low KE_T/n_q region ($KE_T/n_q < 0.1$ GeV), protons sit below the common scaling fit and rise above the fit at moderate KE_T/n_q . These deviations systematically change with centrality, i.e. the proton v_2 is smaller than pion v_2 at low KE_T/n_q in the most central Au+Au collisions at 200 GeV, while the proton v_2 becomes larger than pion v_2 in peripheral collisions. The proton v_2 is also larger than the pion v_2 at low KE_T/n_q in 200 GeV Cu+Cu peripheral collisions. The proton and pion v_2 become comparable in central Cu+Cu collisions. It is noted that the location where the proton and pion v_2 flows are comparable occurs at a similar number of participants N_{part} for Au+Au and Cu+Cu. This could be explained by an increase in radial flow as a function of the number of participants, which effectively reduces the proton v_2 relative to the pion v_2 for a given p_T [40].

533

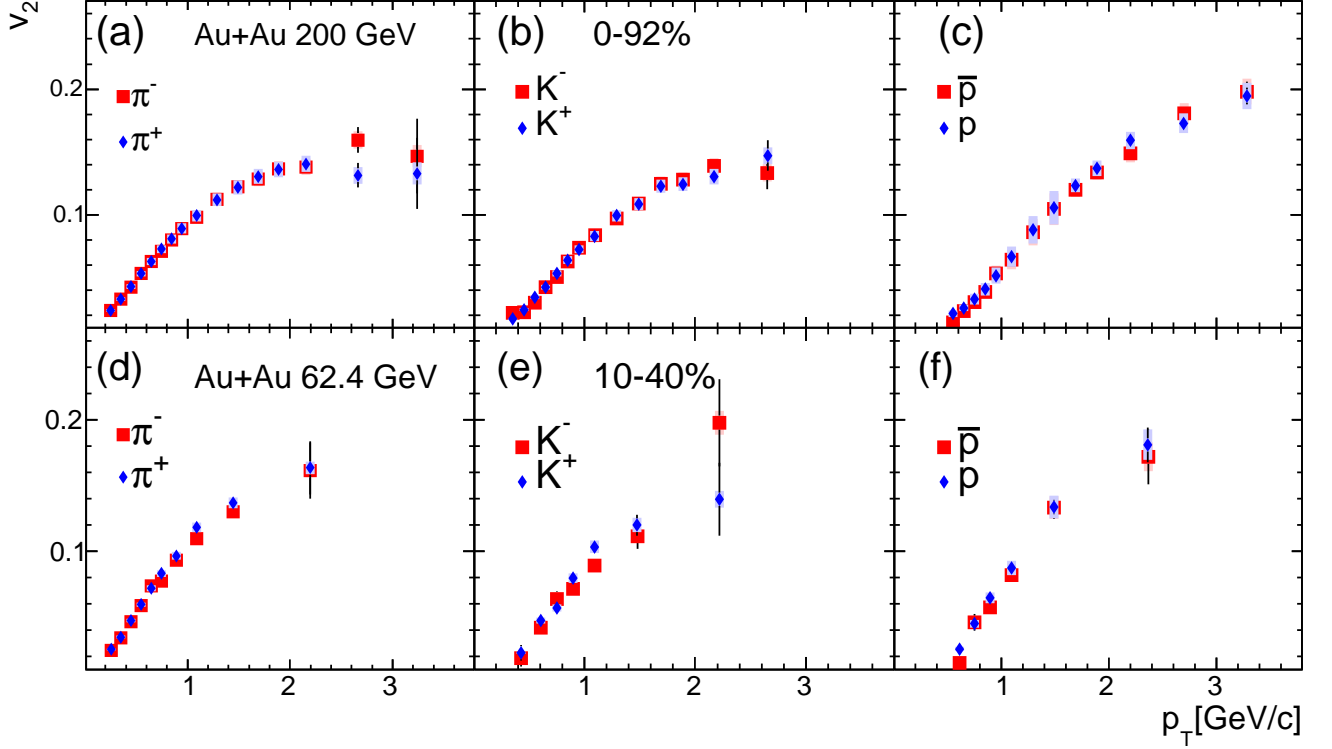


FIG. 16. (Color online) Comparison of the v_2 of particles, antiparticles, for a minimum bias sample 0%–92% at 200 GeV and 10%–40% central at 62.4 GeV in Au+Au collisions. The lines for each point indicate the statistical uncertainties, and the boxes are systematic uncertainties. In many cases, the systematic uncertainties are smaller than the symbols.

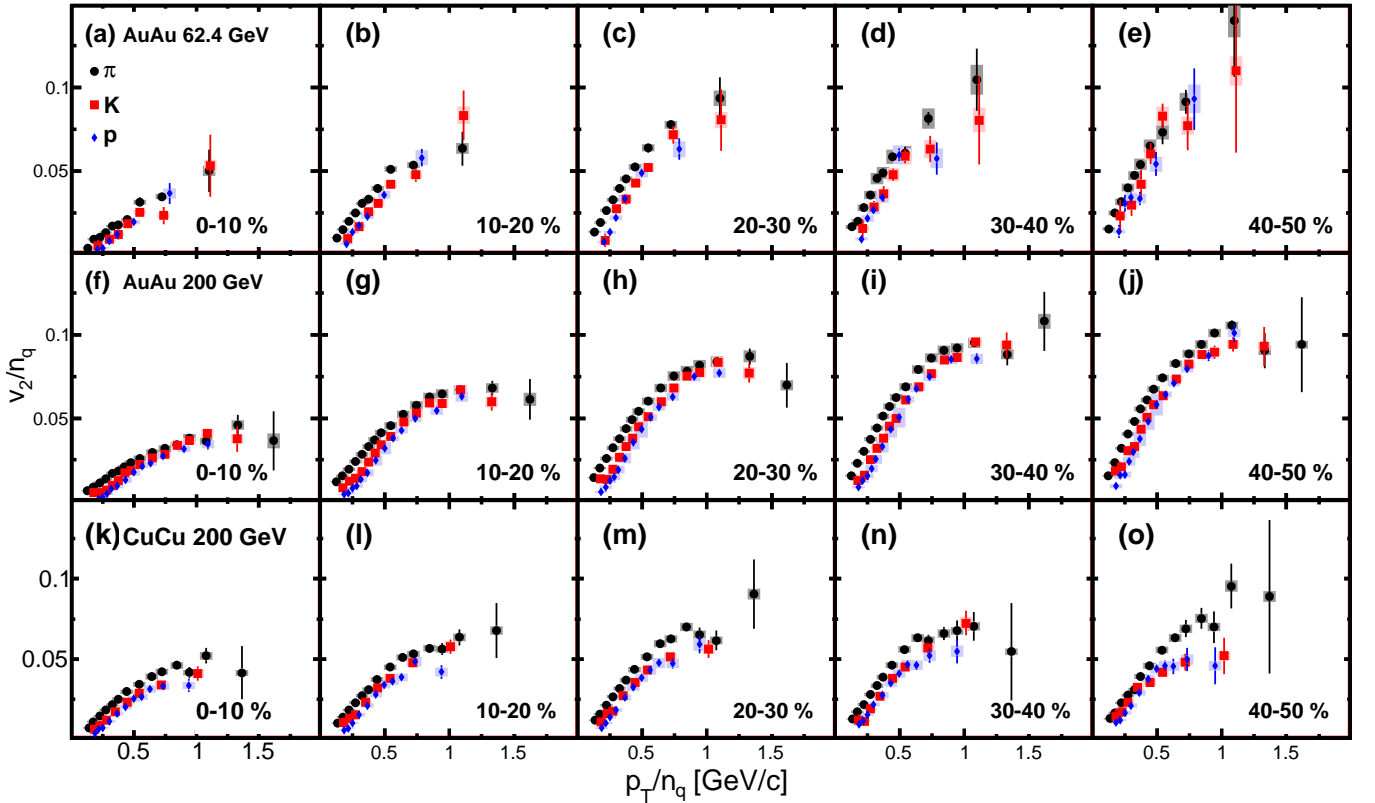


FIG. 17. (Color online) The ratio v_2/n_q vs. p_T/n_q for $\pi/K/p$ emitted from Au+Au at 62.4 and 200 GeV and Cu+Cu at 200 GeV collisions for the centralities indicated. The lines for each point indicate the statistical uncertainties, and the boxes are systematic uncertainties. In many cases, the systematic uncertainties are smaller than the symbols.

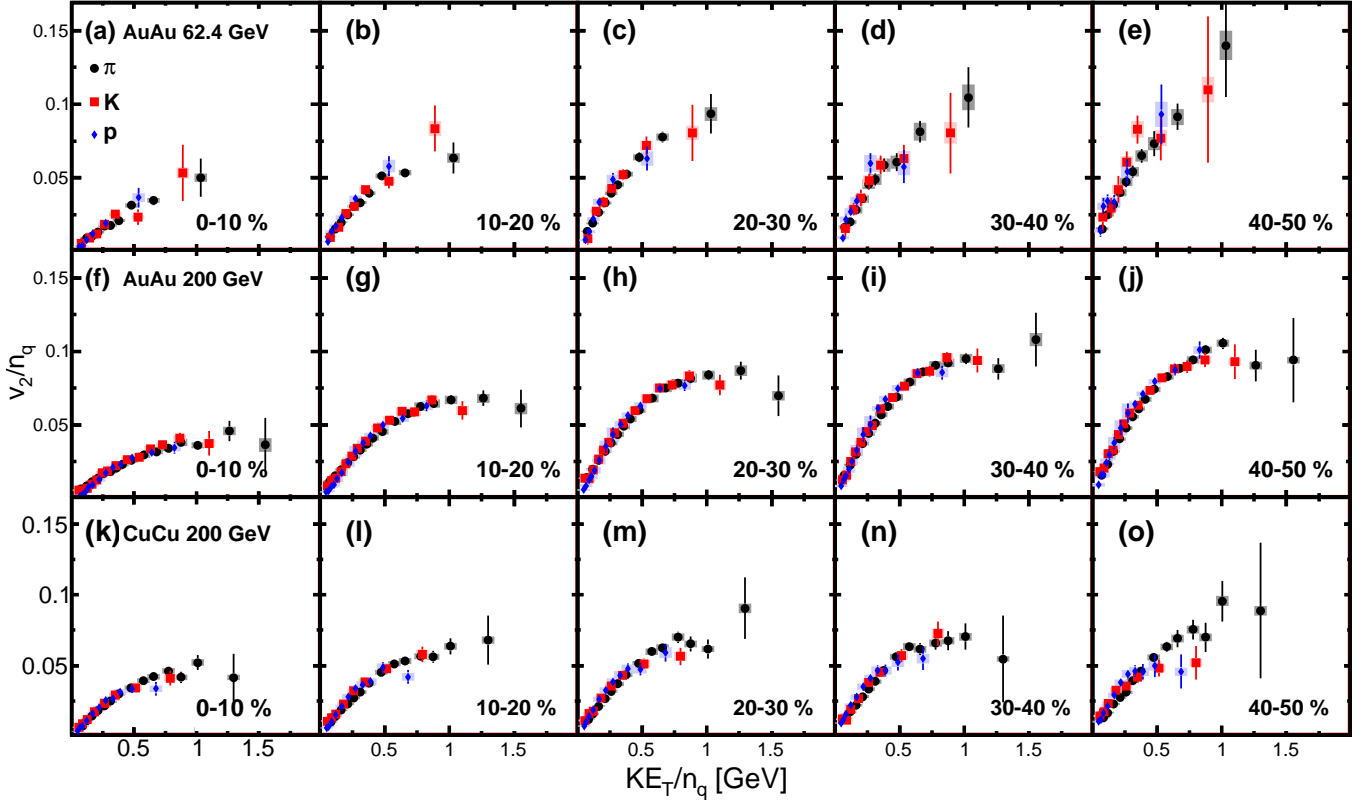


FIG. 18. (Color online) The ratio v_2/n_q vs. KE_T/n_q for $\pi/K/p$ emitted from Au+Au at 62.4 and 200 GeV and Cu+Cu at 200 GeV collisions for the centralities indicated. The lines for each point indicate the statistical uncertainties and the boxes are systematic uncertainties. In many cases, the systematic uncertainties are smaller than the symbols.

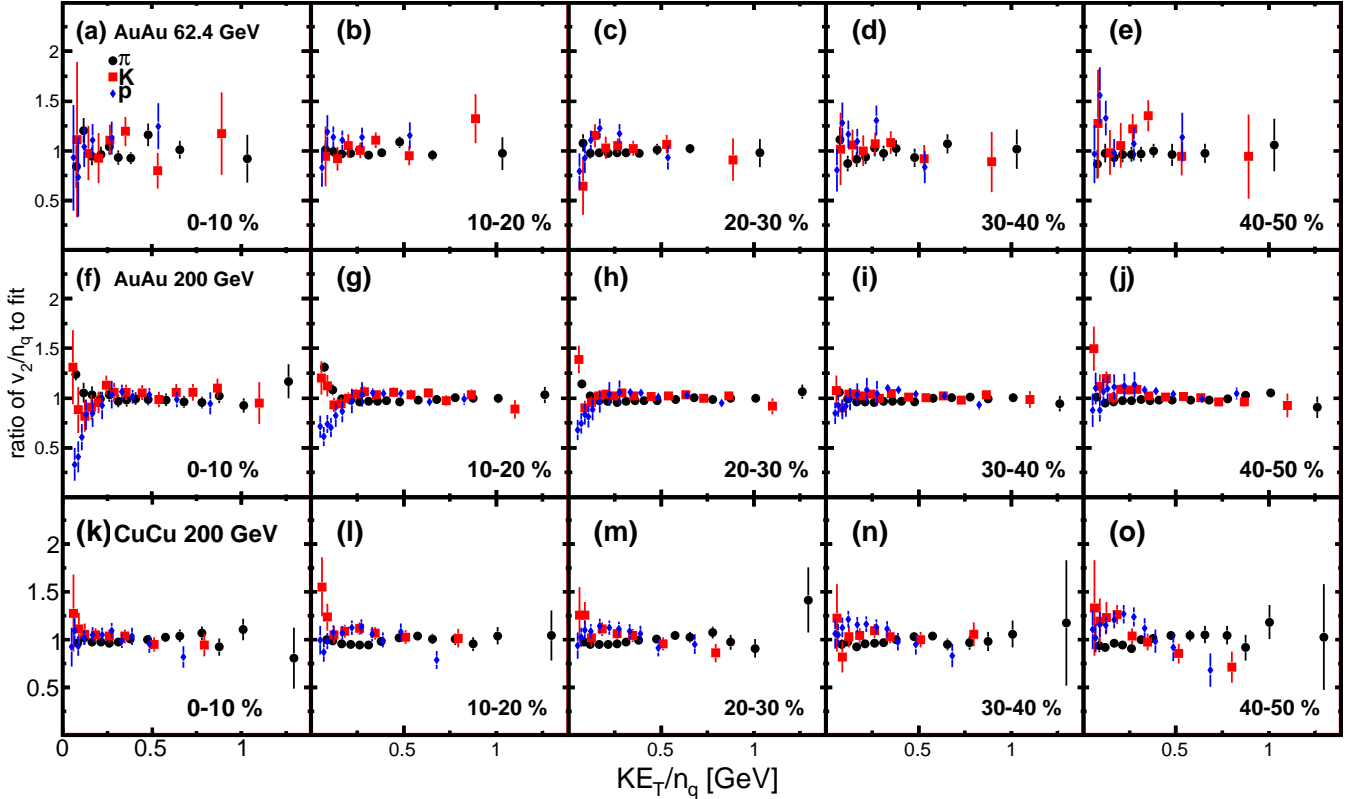


FIG. 19. (Color online) The ratio of v_2/n_q vs. KE_T/n_q to the fit for $\pi/K/p$ emitted from Au+Au at 62.4 and 200 GeV and Cu+Cu at 200 GeV collisions for the centralities indicated. The lines for each point indicate the statistical uncertainties.

534 For Cu+Cu collisions at 200 GeV, the bottom five panels of Figs. 17 and 18 show the v_2/n_q vs. p_T/n_q and KE_T/n_q ,
 535 respectively for $\pi/K/p$ emitted from Cu+Cu collisions at 200 GeV for the five centrality bins: 0%–10%, 10%–20%,
 536 20%–30%, 30%–40% and 40%–50%. For the smaller system of Cu+Cu at 200 GeV (the bottom row of Fig. 18), quark
 537 number with KE_T scalings reduces the spread in v_2 values better than p_T scaling in Fig. 17, especially for the more
 538 central collisions between 0%–40%. For peripheral Cu+Cu collisions, the number of quark scaling with KE_T does
 539 not work well. The deviation from n_q scaling seems to be largest at peripheral collisions, i.e. at 40%–50%, especially
 540 between pions and protons.

541 We examine in more detail the scaling at low KE_T in the 62.4 GeV data in stages. First, the left panel in Fig. 20
 542 summarizes the unscaled v_2 data from 10%–40% central Au+Au collisions at 62.4 GeV. The v_2 values are broadly
 543 spread in their magnitude. A reduction in spread is observed in the right panel when n_q , the number of valence
 544 quarks, is used as a scaling. However the scaled v_2 values do not collapse to a universal curve. Figure 21 does show
 545 a better scaling with KE_T/n_q .

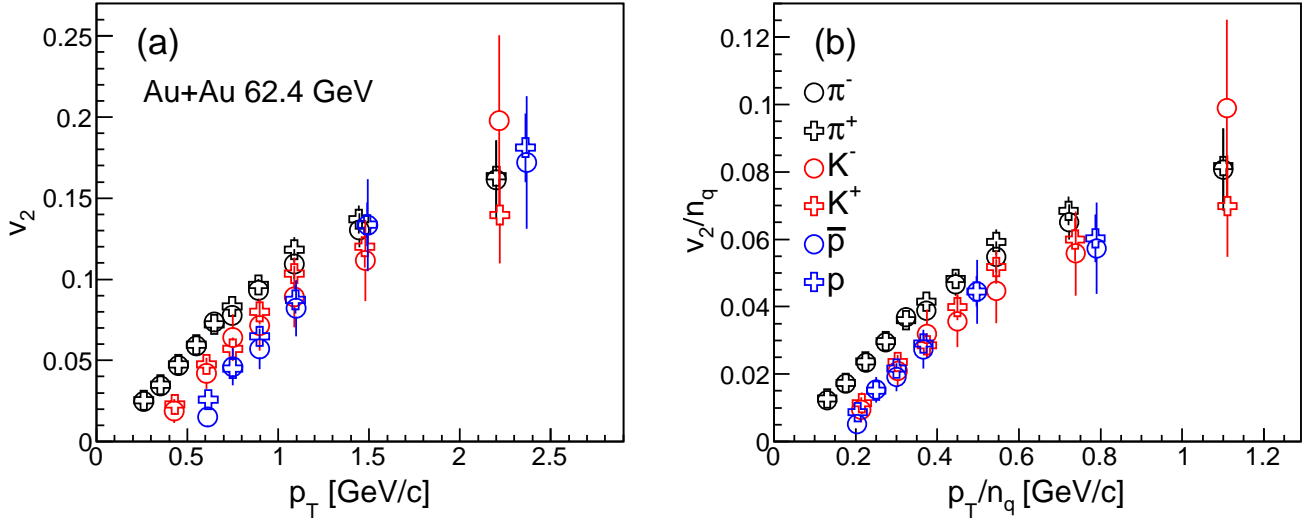


FIG. 20. (Color online) The left panel shows v_2 vs. p_T , the right panel is the ratio v_2/n_q vs. p_T/n_q for the indicated hadrons emitted from 10%–40 % central Au+Au collisions in Au+Au at 62.4 GeV. The error bars include both systematic and statistical uncertainties.

546 Overall, the combined $n_q - KE_T$ scaling works well (typical deviations less than 20%) for $0.1 < KE_T/n_q < 1$ GeV,
 547 indicating that the elliptic collective motion is created at a level consistent with constituent quarks both at 62.4 GeV
 548 in Au+Au and at 200 GeV in Cu+Cu.

549 D. Universal v_2 scaling

550 We consider a universal v_2 scaling for all the v_2 measurements in this paper for identified hadrons between
 551 $0.1 < KE_T/n_q < 1$ GeV. Within a given collision system, i.e. each centrality bin for each set of Au+Au and
 552 Cu+Cu collisions, we first apply quark number n_q scaling and KE_T scaling. Then we apply the eccentricity normal-
 553 ization and $N_{\text{part}}^{1/3}$ scaling for each colliding system. Because we have observed that v_2 saturates with beam energy
 554 between 62–200 GeV, we do not apply any scaling with beam energy. The v_2 data with the four factors applied (quark
 555 number scaling, KE_T scaling, eccentricity normalization and $N_{\text{part}}^{1/3}$ scaling) are shown as a function of KE_T/n_q in
 556 Fig. 22, which includes data from Au+Au at 200 GeV, Au+Au at 62.4 GeV and Cu+Cu at 200 GeV at five centrality
 557 bins over 0%–50% in 10% steps for each system. There are 45 v_2 data sets in total. The combined data is fit with a
 558 single 3rd-order-polynomial, producing a $\chi^2/NDF = 1034/490 = 2.11$ (including both statistical and systematic un-
 559 certainties). Note there is no Cu+Cu 62.4 GeV data in Fig. 22, because there were insufficient statistics to determine
 560 v_2 for identified particles.

561 If we apply the $N_{\text{coll}}^{1/3}$ scaling to the same data sets instead of $N_{\text{part}}^{1/3}$ scaling, we obtain $\chi^2/NDF = 2643/490 = 5.39$.
 562 Therefore, $N_{\text{part}}^{1/3}$ is a better scaling factor than $N_{\text{coll}}^{1/3}$. As we mentioned Section V C, there are some deviations from
 563 the quark number and KE_T scalings, therefore this $N_{\text{part}}^{1/3}$ normalized curve is not perfectly a single line. Further

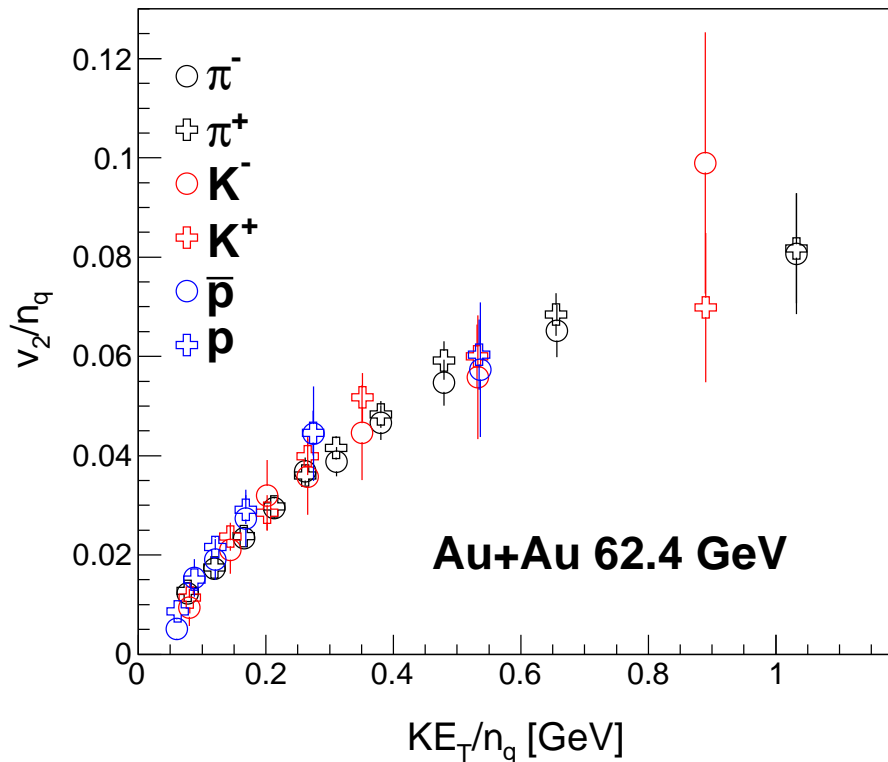


FIG. 21. (Color online) The ratio v_2/n_q vs. KE_T/n_q for the indicated hadrons emitted from 10%-40% central Au+Au collisions at 62.4 GeV. The error bars include both systematic and statistical uncertainties.

564 investigation of these deviations would require higher precision measurements.

565

VI. SUMMARY AND CONCLUSION

566 We have measured the strength of the elliptic anisotropy, v_2 , for inclusive charged hadrons and identified charged
 567 hadrons ($\pi/K/p$) in Au+Au and Cu+Cu collisions at $\sqrt{s_{NN}} = 200$ and 62.4 GeV to study the dependence of v_2 on
 568 collision energy, species and centrality. Results of this systematic study reveal the following features. Comparisons
 569 between 200 and 62.4 GeV collisions demonstrate that v_2 as a function of p_T does not depend on beam energy in
 570 Au+Au. In Cu+Cu, the v_2 at 62.4 GeV is slightly lower than that at 200 GeV.

571 One possibility for the lower v_2 values 62.4 GeV in Cu+Cu is less complete thermalization in small systems at lower
 572 beam energies. At least two types of theoretical models have been used to investigate the question of incomplete
 573 thermalization for systems formed at RHIC. Borghini argues that because v_2/ε depends on dN/dy [41], the systems
 574 formed at RHIC are not fully thermalized during the time when v_2 develops. Borghini argues that this dN/dy
 575 dependence can be interpreted as dependence on a Knudsen number representing incomplete thermalization. Recent
 576 hydrodynamical models that include shear viscosity and initial fluctuations [11–13] effectively include nonequilibrium
 577 effects through the finite viscosity. Using a different non-equilibrium approach, microscopic transport models [42]
 578 solve the relativistic Boltzmann equation. Both the viscous hydrodynamical and the Boltzmann transport models
 579 can be tested with our two observation that the v_2 at Cu+Cu at 62.4 GeV is slightly lower than that at 200 GeV,
 580 and that the measured universal scaling breakdowns in peripheral Cu+Cu.

581 For various hadron species the measured v_2 results as a function of p_T are well scaled by quark number. Interestingly,
 582 it appears that this scaling holds also for higher orders in azimuthal anisotropy [43]. The KE_T scaling performs better
 583 than p_T scaling, particularly in the intermediate transverse momentum region ($p_T = 1-4$ GeV/c). This scaling property
 584 suggests that the matter flows with quark-like degrees of freedom, and therefore is consistent with the formation of
 585 QGP matter [7]. A small deviation from KE_T scaling can be seen for both Au+Au and Cu+Cu collisions, and this
 586 deviation depends on the number of participants N_{part} . This deviation might indicate a restricted region where KE_T
 587 scaling works well, possibly dependent on the strength of the radial flow.

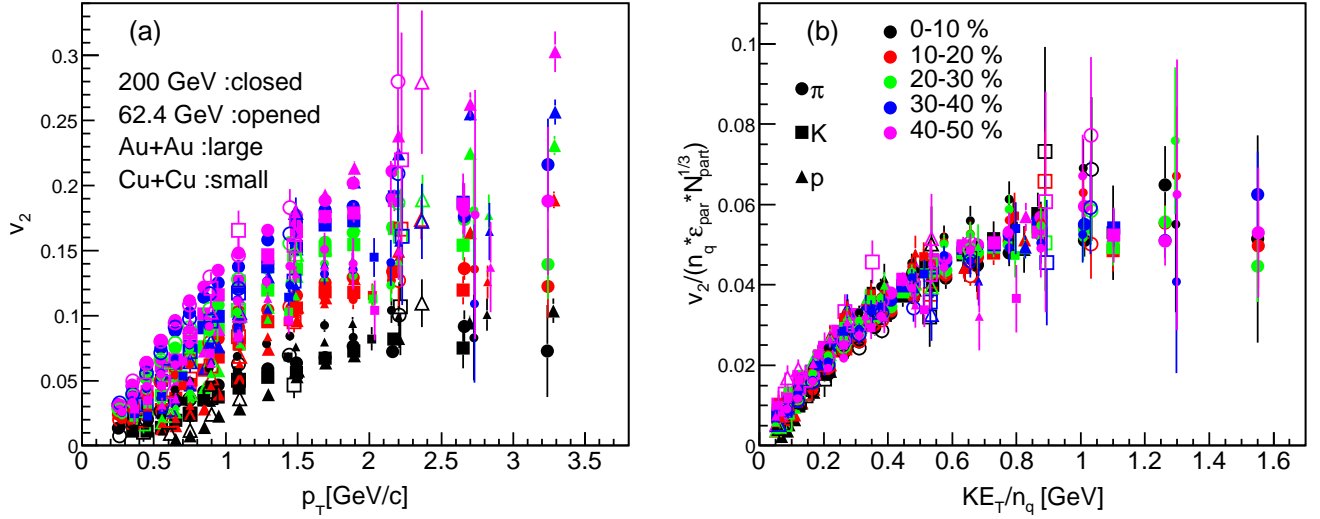


FIG. 22. (Color online) The left panel shows v_2 vs. p_T and the right panel shows $v_2/(\varepsilon \cdot N_{\text{part}}^{1/3} \cdot n_q)$ vs. KE_T/n_q for $\pi/K/p$ in Au+Au at 200 GeV, in Au+Au at 62.4 GeV and in Cu+Cu at 200 GeV for five centrality bins over 0%–50% in 10% steps for each system. There are 45 data sets in each panel.

588 For both Au+Au to Cu+Cu collisions, we confirm that v_2 can be normalized by participant eccentricity (ε) [30].
 589 This indicates that the effect of initial geometrical anisotropy can be partially removed by eccentricity normalization.
 590 However, v_2 normalized by ε still depends on N_{part} , v_2 is not fully determined by ε alone and we have empirically
 591 found that v_2/ε is proportional to $N_{\text{part}}^{1/3}$. The initial participant size $N_{\text{part}}^{1/3}$, is related to a length scale or an expansion
 592 time scale. Taking account all scalings and normalization, the data “ $v_2/n_q/\varepsilon/N_{\text{part}}^{1/3}$ vs. KE_T/n_q ” lie on a universal
 593 curve for $0.1 < KE_T/n_q < 1$ GeV.

594 ACKNOWLEDGMENTS

595 We thank the staff of the Collider-Accelerator and Physics Departments at Brookhaven National Laboratory and
 596 the staff of the other PHENIX participating institutions for their vital contributions. We acknowledge support from
 597 the Office of Nuclear Physics in the Office of Science of the Department of Energy, the National Science Founda-
 598 tion, Abilene Christian University Research Council, Research Foundation of SUNY, and Dean of the College of
 599 Arts and Sciences, Vanderbilt University (U.S.A), Ministry of Education, Culture, Sports, Science, and Technology
 600 and the Japan Society for the Promotion of Science (Japan), Conselho Nacional de Desenvolvimento Científico e
 601 Tecnológico and Fundação de Amparo à Pesquisa do Estado de São Paulo (Brazil), Natural Science Foundation of
 602 China (P. R. China), Ministry of Education, Youth and Sports (Czech Republic), Centre National de la Recherche
 603 Scientifique, Commissariat à l’Énergie Atomique, and Institut National de Physique Nucléaire et de Physique des
 604 Particules (France), Bundesministerium für Bildung und Forschung, Deutscher Akademischer Austausch Dienst, and
 605 Alexander von Humboldt Stiftung (Germany), National Science Fund, OTKA, Károly Róbert University College, and
 606 the Ch. Simonyi Fund (Hungary), Department of Atomic Energy (India), Israel Science Foundation (Israel), National
 607 Research Foundation and WCU program of the Ministry Education Science and Technology (Korea), Ministry of Ed-
 608 ucation and Science, Russian Academy of Sciences, Federal Agency of Atomic Energy (Russia), VR and Wallenberg
 609 Foundation (Sweden), the U.S. Civilian Research and Development Foundation for the Independent States of the
 610 Former Soviet Union, the US-Hungarian NSF-OTKA-MTA, and the US-Israel Binational Science Foundation.

- 611 [1] K. Adcox *et al.* (PHENIX Collaboration), “Formation of dense partonic matter in relativistic nucleus-nucleus collisions at
 612 RHIC: Experimental evaluation by the PHENIX Collaboration,” Nucl. Phys. A **757**, 184 (2005).
 613 [2] J. Adams *et al.* (STAR Collaboration), “Experimental and theoretical challenges in the search for the quark gluon plasma:
 614 The STAR Collaboration’s critical assessment of the evidence from RHIC collisions,” Nucl. Phys. A **757**, 102 (2005).

- [3] B. B. Back *et al.* (PHOBOS Collaboration), “The PHOBOS perspective on discoveries at RHIC,” Nucl. Phys. A **757**, 28 (2005).
- [4] I. Arsene *et al.* (BRAHMS Collaboration), “Quark gluon plasma and color glass condensate at RHIC? The Perspective from the BRAHMS experiment,” Nucl. Phys. A **757**, 1 (2005).
- [5] S. S. Adler *et al.* (PHENIX Collaboration), “Elliptic flow of identified hadrons in Au+Au collisions at $\sqrt{s_{NN}} = 200$ GeV,” Phys. Rev. Lett. **91**, 182301 (2003).
- [6] M. Bleicher and H. Stoecker, “Anisotropic flow in ultrarelativistic heavy ion collisions,” Phys. Lett. B **526**, 309 (2002).
- [7] A. Adare *et al.* (PHENIX Collaboration), “Scaling properties of azimuthal anisotropy in Au+Au and Cu+Cu collisions at $\sqrt{s} = 200$ GeV,” Phys. Rev. Lett. **98**, 162301 (2007).
- [8] A. Adare *et al.* (PHENIX Collaboration), “Deviation from quark-number scaling of the anisotropy parameter v_2 of pions, kaons, and protons in Au+Au collisions at $\sqrt{s_{NN}}=200$ GeV,” Phys. Rev. C **85**, 064914 (2012).
- [9] U. Heinz and R. Snellings, “Collective flow and viscosity in relativistic heavy-ion collisions,” Ann. Rev. Nucl. Part. Sci. **63**, 123 (2013).
- [10] J.-Y. Ollitrault, “Anisotropy as a signature of transverse collective flow,” Phys. Rev. D **46**, 229 (1992).
- [11] H. Niemi, G.S. Denicol, P. Huovinen, E. Molnar, and D.H. Rischke, “Influence of a temperature-dependent shear viscosity on the azimuthal asymmetries of transverse momentum spectra in ultrarelativistic heavy-ion collisions,” Phys. Rev. C **86**, 014909 (2012).
- [12] H. Song, S. A. Bass, U. Heinz, T. Hirano, and C. Shen, “Hadron spectra and elliptic flow for 200 A GeV Au+Au collisions from viscous hydrodynamics coupled to a Boltzmann cascade,” Phys. Rev. C **83**, 054910 (2011); *Erratum: ibid* **86**, 059903E (2012).
- [13] R. A. Soltz, I. Garishvili, M. Cheng, B. Abelev, A. Glenn, J. J. Newby, L. A. LindenLevy, and S. Pratt, “Constraining the initial temperature and shear viscosity in a hybrid hydrodynamic model of $\sqrt{s_{NN}}=200$ GeV Au+Au collisions using pion spectra, elliptic flow, and femtoscopic radii,” Phys. Rev. C **87**, 044901 (2013).
- [14] K Aamodt *et al.* (ALICE Collaboration), “Charged-particle multiplicity density at mid-rapidity in central Pb-Pb collisions at $\sqrt{s_{NN}}=2.76$ TeV,” Phys. Rev. Lett. **105**, 252301 (2010).
- [15] G. Aad *et al.* (ATLAS Collaboration), “Measurement of the azimuthal anisotropy for charged particle production in $\sqrt{s_{NN}}=2.76$ TeV lead-lead collisions with the ATLAS detector,” Phys. Rev. C **86**, 014907 (2012).
- [16] S. Chatrchyan *et al.* (CMS Collaboration), “Measurement of the elliptic anisotropy of charged particles produced in PbPb collisions at $\sqrt{s_{NN}}=2.76$ TeV,” Phys. Rev. C **87**, 014902 (2013).
- [17] B. Abelev *et al.* (ALICE Collaboration), “Anisotropic flow of charged hadrons, pions and (anti-)protons measured at high transverse momentum in Pb-Pb collisions at $\sqrt{s_{NN}}=2.76$ TeV,” Phys. Lett. B **719**, 18 (2013).
- [18] B. B. Abelev *et al.* (ALICE Collaboration), “Elliptic flow of identified hadrons in Pb-Pb collisions at $\sqrt{s_{NN}} = 2.76$ TeV,” ArXiv:1405.4632.
- [19] L. Adamczyk *et al.* (STAR Collaboration), “Elliptic flow of identified hadrons in Au+Au collisions at $\sqrt{s_{NN}} = 7.7-62.4$ GeV,” Phys. Rev. C **88**, 014902 (2013).
- [20] B. I. Abelev *et al.* (STAR Collaboration), “Charged and strange hadron elliptic flow in Cu+Cu collisions at $\sqrt{s_{NN}} = 62.4$ and 200 GeV,” Phys. Rev. C **81**, 044902 (2010).
- [21] A. Adare *et al.* (PHENIX Collaboration), “Quadrupole Anisotropy in Dihadron Azimuthal Correlations in Central $d+Au$ Collisions at $\sqrt{s_{NN}}=200$ GeV,” Phys. Rev. Lett. **111**, 212301 (2013).
- [22] V. Khachatryan *et al.* (CMS Collaboration), “Observation of Long-Range Near-Side Angular Correlations in Proton-Proton Collisions at the LHC,” J. High Energy Phys. **1009**, 091 (2010).
- [23] S. Chatrchyan *et al.* (CMS Collaboration), “Observation of long-range near-side angular correlations in proton-lead collisions at the LHC,” Phys. Lett. B **718**, 795 (2013).
- [24] S. Afanasiev *et al.* (PHENIX Collaboration), “Systematic Studies of Elliptic Flow Measurements in Au+Au Collisions at $\sqrt{s} = 200$ GeV,” Phys. Rev. C **80**, 024909 (2009).
- [25] K. Adcox *et al.* (PHENIX Collaboration), “PHENIX detector overview,” Nucl. Instrum. Methods Phys. Res., Sec. A **499**, 469 (2003).
- [26] M. Aizawa *et al.* (PHENIX Collaboration), “PHENIX central arm particle ID detectors,” Nucl. Instrum. Methods Phys. Res., Sec. A **499**, 508 (2003).
- [27] K. Adcox *et al.* (PHENIX Collaboration), “Construction and performance of the PHENIX pad chambers,” Nucl. Instrum. Methods Phys. Res., Sec. A **497**, 263 (2003).
- [28] L. Aphecetche *et al.* (PHENIX Collaboration), “PHENIX calorimeter,” Nucl. Instrum. Methods Phys. Res., Sec. A **499**, 521 (2003).
- [29] S. S. Adler *et al.* (PHENIX Collaboration), “Systematic studies of the centrality and $\sqrt{s_{NN}}$ dependence of the $d E(T) / d \eta$ and $d(N(\text{ch}) / d \eta$ in heavy ion collisions at mid-rapidity,” Phys. Rev. C **71**, 034908 (2005).
- [30] B. Alver *et al.* (PHOBOS Collaboration), “System size, energy, pseudorapidity, and centrality dependence of elliptic flow,” Phys. Rev. Lett. **98**, 242302 (2007).
- [31] M. L. Miller, K. Reygers, Stephen J. Sanders, and Peter Steinberg, “Glauber modeling in high energy nuclear collisions,” Ann. Rev. Nucl. Part. Sci. **57**, 205 (2007).
- [32] J. T. Mitchell *et al.* (PHENIX Collaboration), “Event reconstruction in the PHENIX central arm spectrometers,” Nucl. Instrum. Methods Phys. Res., Sec. A **482**, 491 (2002).
- [33] S. S. Adler *et al.* (PHENIX Collaboration), “High p_T charged hadron suppression in Au + Au collisions at $\sqrt{s_{NN}} = 200$ GeV,” Phys. Rev. C **69**, 034910 (2004).

- 678 [34] S. S. Adler *et al.* (PHENIX Collaboration), “Jet structure from dihadron correlations in d+Au collisions at $\sqrt{s_{NN}} =$
679 200 GeV,” *Phys. Rev. C* **73**, 054903 (2006).
- 680 [35] A. M. Poskanzer and S. A. Voloshin, “Methods for analyzing anisotropic flow in relativistic nuclear collisions,” *Phys. Rev.*
681 *C* **58**, 1671 (1998).
- 682 [36] A. Adare *et al.* (PHENIX Collaboration), “Elliptic and hexadecapole flow of charged hadrons in Au+Au collisions at
683 $\sqrt{s_{NN}}=200$ GeV,” *Phys. Rev. Lett.* **105**, 062301 (2010).
- 684 [37] S. Afanasiev *et al.* (PHENIX Collaboration), “Kaon interferometric probes of space-time evolution in Au+Au collisions at
685 $\sqrt{s_{NN}} = 200$ GeV,” *Phys. Rev. Lett.* **103**, 142301 (2009).
- 686 [38] C. Adler *et al.* (STAR Collaboration), “Elliptic flow from two and four particle correlations in Au+Au collisions at $\sqrt{s_{NN}}$
687 $= 130$ GeV,” *Phys. Rev. C* **66**, 034904 (2002).
- 688 [39] B. I. Abelev *et al.* (STAR Collaboration), “Mass, quark-number, and $\sqrt{s_{NN}}$ dependence of the second and fourth flow
689 harmonics in ultra-relativistic nucleus-nucleus collisions,” *Phys. Rev. C* **75**, 054906 (2007).
- 690 [40] S. A. Voloshin, A. M. Poskanzer, and R. Snellings, “Collective phenomena in non-central nuclear collisions,” (2008),
691 arXiv:0809.2949.
- 692 [41] N. Borghini, “Hints of incomplete thermalization in RHIC data,” *Eur. Phys. J. A* **29**, 27 (2006).
- 693 [42] J. Uphoff, F. Senzel, O. Fochler, C. Wesp, Z. Xu, *et al.*, “Elliptic flow and nuclear modification factor in ultrarelativistic
694 heavy-ion collisions within a partonic transport model,” *Phys. Rev. Lett.* **114**, 112301 (2015).
- 695 [43] A. Adare *et al.* (PHENIX Collaboration), “Measurement of the higher-order anisotropic flow coefficients for identified
696 hadrons in Au+Au collisions at $\sqrt{s_{NN}} = 200$ GeV,” ArXiv:1412.1038.